Aerodynamic Analysis of ADEPT SR-1 Forebody

A project presented to
The Faculty of Department of Aerospace Engineering
San Jose State University

in particular fulfillment of the requirement for the degree
Master of Science in Aerospace Engineering

By
Zijing Zheng

August 8, 2023

Approved by

Dr. Derek Lang
Faculty Advisor

Abstract

Aerodynamic Effort of ADEPT Forebody Analysis

Zheng Z. Oriented

The Adaptable Deployable Entry Placement Technology Sounding Rocket One (ADEPT SR-1) experienced an unexpected spike in roll rate during reentry. A computational study was undertaken to analyze the aerodynamic effects on the ADEPT forebody at the peak Mach condition of the SR-1 experiment. The ANSYS Fluent program was employed to simulate the spacecraft's aerodynamic performance. An investigation was carried out through a series of 2D axisymmetric, and 3D model Computational Fluid Dynamics (CFD) simulations in ANSYS Fluent, focusing on the SR-1 forebody geometry. The obtained CFD results were subsequently compared with the dynamic stability data from SR-1 flight articles. This project aims to determine the potential occurrence of unforeseen aerodynamic effects demonstrated by the forebody of the SR-1 at Mach 3..

Acknowledgement

I hold great respect and extend my gratitude to Dr. Derek Lang for his invaluable guidance and inspiration, which played a significant role in the completion of this project. I also wish to express my appreciation to the NASA ADEPT team members, Jeffery Hill, Ashely Korzun, and Ryan McDaniel, for generously sharing their knowledge and expertise.

Table of Content

List of Figure

Symbol

Symbol	Definition	Units (SI)
C	Coefficient	
L	Length	meter
R	Radius	meter
V	Velocity	meter per second
ρ	Density	
A	Area	square meter
Greek Symbol		
α	Angle of Attack	degree
β	Side Slip Angle	degree
Subscripts		
$(\ )_A$	Axial Force	
$(\ )_Y$	Side Force	
$(\ )_N$	Normal Force	
$(\ )_l$	Rolling Moment	
$(\ )_m$	Pitching Moment	
$(\ )_n$	Yawing Moment	
$(\ )_T$	Total	
$(\ )_x$	X - direction	
$(\ )_y$	Y - direction	
$(\ )_z$	Z - direction	
Acronyms		
AOA	Angle of Attack	degree
CoG	Center of Gravity	
CoP	Center of Pressure	
SA	Surface Area	square meter
RA	Roll Angle	degree

1. Introduction

1.1 Motivation

The Adaptive Deplorable Entry and Placement Technology (ADEPT) from NASA introduces a novel semi-rigid, low-ballistic coefficient aeroshell entry concept for executing Entry, Descent, and Landing (EDL) in upcoming planetary entry missions. This innovative approach empowers engineers to devise a foldable, umbrella-like aeroshell that can be accommodated within the spacecraft during space travel, subsequently transitioning into a deployed, nearly rigid, low-ballistic coefficient configuration prior to the EDL phase, as depicted in Figure 1. The ADEPT architecture is scalable, catering to scientific payload deployment or human planetary exploration missions spanning the 1m to 20m diameter class size [1]. A compact ADEPT variant can be integrated as a secondary payload, bolstering primary missions or standing alone in interplanetary endeavors. Alternatively, a full-scale ADEPT could facilitate interplanetary supply delivery for scientific payloads or vehicle deployment. A pivotal objective of ADEPT is furnishing a dependable entry system for in-situ probes, landers, orbiters, and orbiting constellations. The foldable heat shield enhances the vehicle's payload volume capacity. Notably, the NASA Sounding Rocket 1 (SR-1) mission undertook a 0.7m diameter nano-ADEPT system flight experiment, which effectively validated the technology's capabilities through successful deployment and landing [2][3].

In this experiment, ADEPT SR-1 showcased aerodynamic stability sans active control, descending to Mach 0.8 from an altitude of 100 km. It impeccably achieved all mission objectives, encompassing full deployment and acquisition of data required for reconstructing the ADEPT 6-Degree of Freedom model descent trajectory.
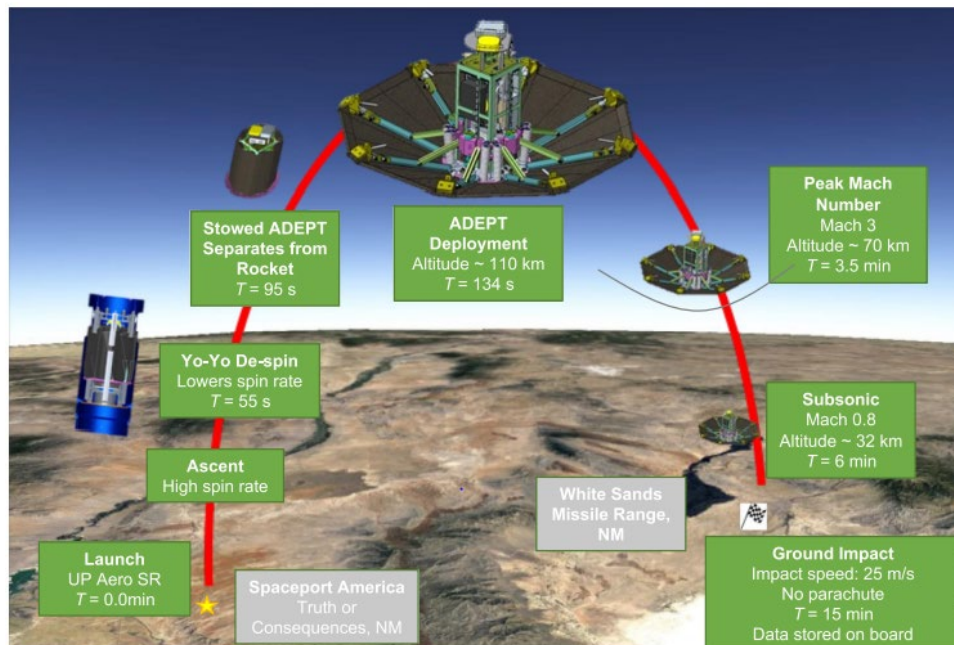
Figure 1. ADEPT SR-1 concept of operation [2]

During the process, ADEPT experienced an unexpected increase in spin rate during supersonic deceleration after reaching peak Mach. This behavior was not predicted in the SR-1 preflight simulation, which could lead to unstable landing or positioning during the EDL phase when ADEPT deploys at higher altitudes for future missions.

The ADEPT flight was predicted by NASA using an Aerodynamic Database (ADB) generated from wind tunnel tests and Computational Fluid Dynamics (CFD) simulations. NASA believes that the unexpected flight dynamics were due to ADEPT's faceted shape. Further calculations and data are required to update the ADB with non-axisymmetric assumptions applied in Computational Fluid Dynamics (CFD) simulations to estimate the rolling moments.
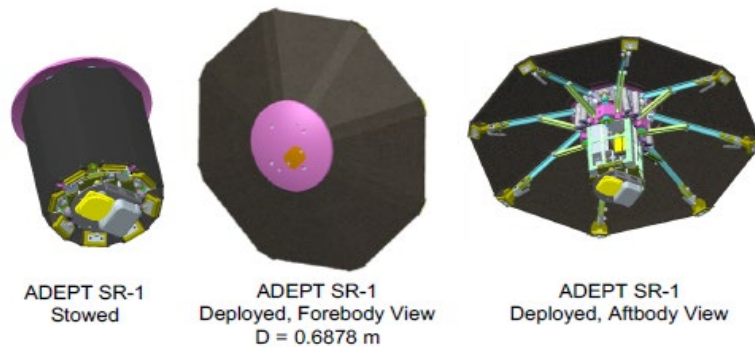
Figure 2, ADEPT SR-1 body view

1.2   Literature review

1.2.1 Reentry Vehicle Heat Shield Geometries

Depending on the mission objective, the design of the heat shield will be determined by the conditions of the planet's atmosphere or the chosen method of entry (i.e., ballistic or lifting). Ballistic entry allows the vehicle to perform a "free fall" entry, which does not require guidance and control, whereas lifting reentry requires active controls using aerodynamic surfaces or propulsive systems.

For a ballistic entry system like ADEPT, the target location needs to be calculated during the orbit before initiating the EDL stage of the mission. However, the vehicle requires a low ballistic factor for direct entry, which necessitates achieving a larger reference area, high drag coefficient, and low mass [5]. These different geometric shapes serve different purposes and offer distinct advantages. The geometry of the spherically blunted cone is defined by the half-angle θ_c, shoulder radius R_s, base radius R_b, and nose radius R_{nose} as shown in Figure 3. The ratio R_{nose} / R_d is a common characteristic in heat shield design. An optimal R_{nose} exists that minimizes the heat transfer of the vehicle, as decreasing the radius of a blunt body leads to an increase in convective heat transfer while maintaining radiative heat transfer. This ratio provides designers the advantage of maintaining the same base radius without restricting the nose radius.
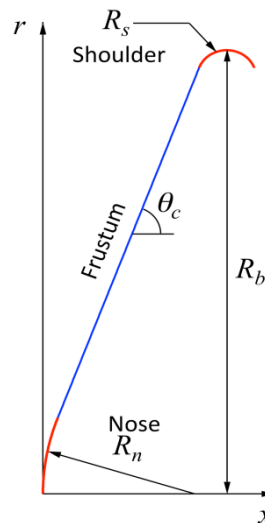
Figure 3, Basic geometry of the spherically blunted cone [6]

As an example, the 70-degree half-angle sphere cone has become a standard geometry for Mars entry vehicles following the success of the Viking mission, as well as for the Mars Exploration Rovers and Mars Science Laboratory, all sharing the same dimensions of θ_c =70°, R_{nose} / R_b =0.25 [7][8]. A study on the geometry of the 70-degree sphere cone concluded that the local surface pressure can be directly affected by the discontinuity at the junction between the spherical nose and the 70-degree conical frustum. The blunted nose helps shift the discontinuity towards the leeward shoulder [6].
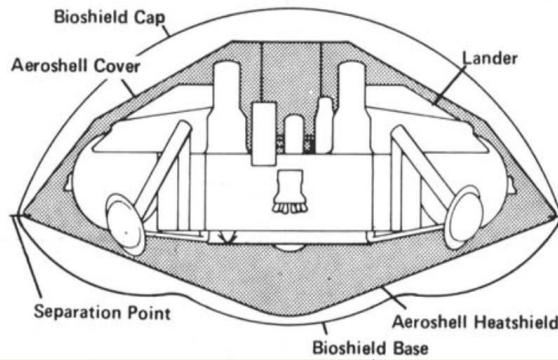
Figure 4, Viking entry capsule

The Stardust Sample Return Capsule performed a successful return with interstellar dust and cometary material collected in space, and created a record of the fastest Earth entry speed of any space missions, 12.6 km/s enter speed and encountered peak deceleration of 34 g. In the meantime, the capsule presented sufficient aerodynamic stability with a true angle of attack of 5° or less when it down to Mach 12 region. The Stardust SRC has a similar design but a smaller size to Viking with a smaller θ_c of 60° sphere cone and over all 0.81 m diameter [9].

The Hypersonic Inflatable Aerodynamic Decelerator (HIAD) involves different diameter inflatable balloon rings with special fabric stacking each other to forma a spherical cone heat shield for the payload, and the concept result was demonstrated in the Inflatable Re-entry Vehicle Experiement-3 in the spring of 2012. The IRVE-3 experienced force up 20 G with a recorded temperature of 1,000 °F and entered Earth's atmosphere at Mach 10. Figure 5 shows the configuration of the IRVE-3 with a diameter of 3m and θ_c of 60°. [10]
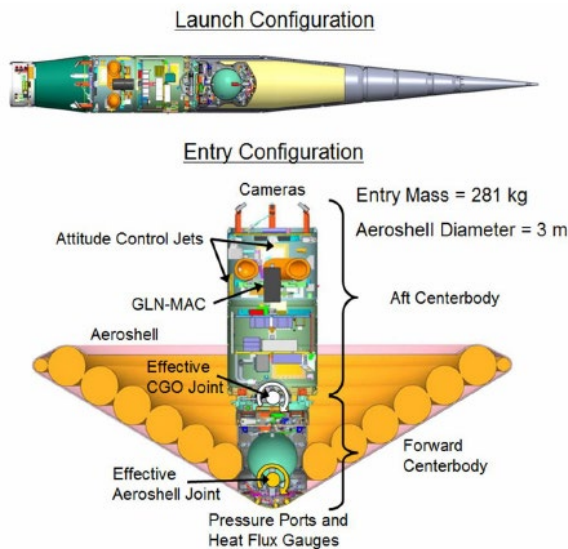
Figure 5. IRVE-3 configuration

The Slotted Compression Ramp (SCRAMP) presents a unique design in which the payload is located in the long cylindrical forebody with a hemispherical nose. It is attached to a θ_c of 70° aft flare with a high half-cone angle, similar to the rest of the vehicle. Within the aft flare, the compression ramp leads to flow recirculation, producing drag force for the vehicle. Additionally, some slots are placed within the aft flare to minimize flow recirculation, which increases the overall drag for the vehicle [11]. This design is similar to the IRVE-3 but with a different position for performing its entry function.

1.2.2 ADEPT Heat Shield Geometry

The ADEPT is a decelerator with a rigid ribbed structure covered by a 3D-woven carbon fabric, which deploys outside the atmosphere before reentry. The basic structure of the ADEPT is outlined in Figure 6 and contains four primary structural components: nose cap, ribs, struts, and the main body. The lower and upper rings of the main body are connected by a truss structure. The lower ring provides support for the lower end of the rib support structures and acts as an outer structure for the secondary payload, while the upper ring serves as an attachment slot for the nose cap. The nose cap functions as the leading edge of the ADEPT with a shape of a sphere-cone to facilitate flow transition for the vehicle. The geometry of the aeroshell determines the number of ribs for the entire structure of the tensioned fabric framework. The struts are installed in pairs to support the ribs and transfer the aerodynamic load from the carbon fabric to the main lower ring [12].
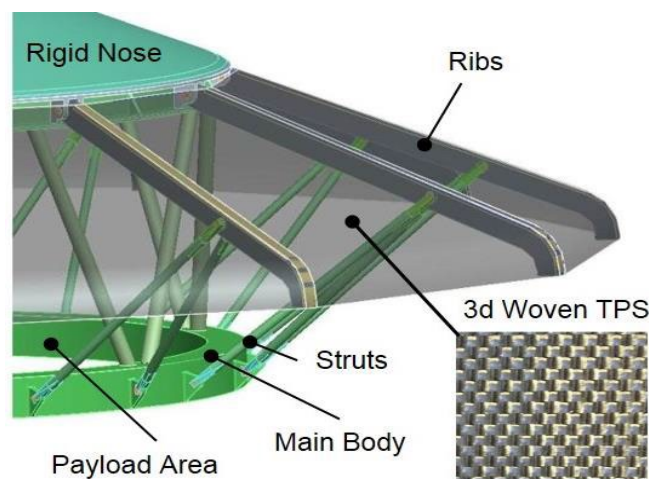
Figure 6, Basic structure of ADEPT

The design of the ADEPT SR-1 heat shield consists of an eight-sided, faceted cone with a 70-degree half-angle and a spherical cone as the nose cap, as shown in Figure 7. When viewed from the aft body of the deployed ADEPT, the main payload is exposed to the environment without significant protection, unlike most space capsules. Due to its use for a 3U CubeSat payload, the diameter of the aeroshell is 0.69 m from rib tip to rib tip, with a reference area of 0.37 m^2. The vehicle's ballistic coefficient is approximately 20 kg/ m^2, with a total mass of 11 kg [2].
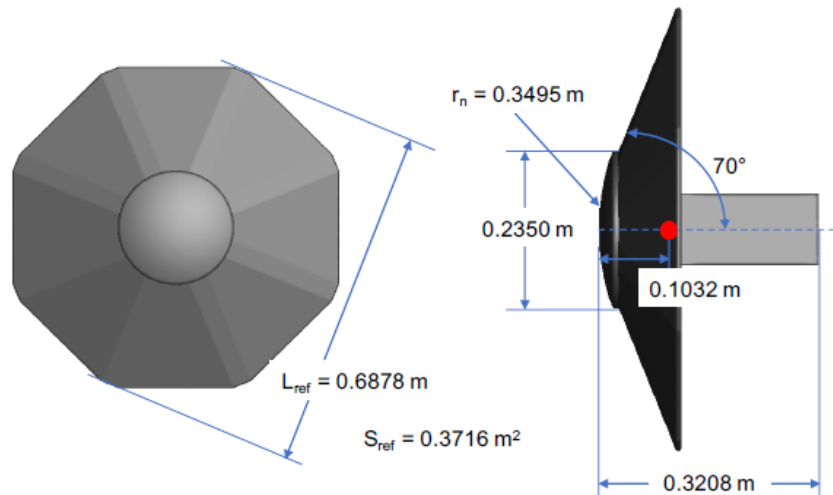
Figure 7, ADEPT SR-1 geometry [2]
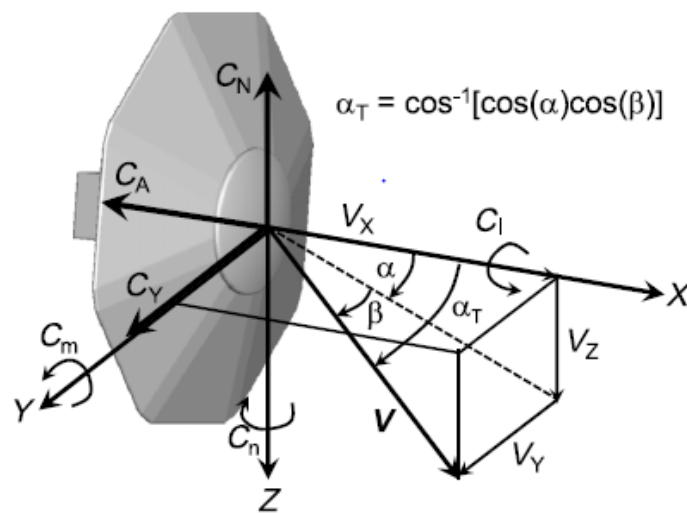
Figure 8. ADEPT coordinates frame [2]

The conventional blunt body heat shield has a more uniform flow field and heat distribution than the ADEPT due to its unique structural design and material. As shown in Figure 9, the flow of the forebody of a conventional heat shield is evenly spread out, whereas in comparison, the flow field of the ADEPT is directed and guided by the structure's ribs. This implies that the design of the ribs, including their length, width, and number, becomes crucial for the overall flow field and heat flux distribution. With flow separation caused by the structure, the discontinuous flow field can indirectly create pressure differences that lead to aerodynamic instability for overall vehicle control at different angles of attack and speeds. The ADEPT SR-1 is not axisymmetric, which makes CFD simulations less predictable and accurate, given the insufficient data for non-axisymmetric heat shields and a wide range of angles of attack.
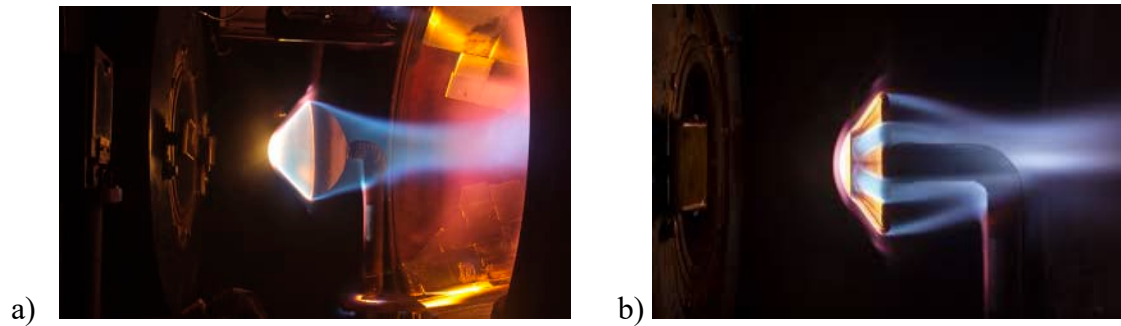
Figure. 9 Aeroshell Comparison of 1) conventional aeroshell geometry flow field 2) ADEPT aeroshell geometry flow field. [22]

1.2.3   SR-1 Pre-Flight Simulation Result

The flight simulation is based on NASA's ADB, which covers different flight regimes including freestream, subsonic, and supersonic. NASA utilized the unstructured Three-Dimensional (US3D) CFD program for the supersonic regime aerodynamic solution, resulting in expected unsteady results due to the separated wake flow in the aft body. Figure 10 clearly demonstrates the dominant influence of forebody pressure on the vehicle's aerodynamics. As no ground test data for the faceted ADEPT SR-1 shape under such flight conditions was available, this CFD supersonic regime solution was used as the static aerodynamic database in the trajectory simulation. Figure 11 presents the nominal continuum supersonic static aerodynamic data with three different angles of attack (AOA). Due to the ADEPT SR-1's faceted shape, the CFD coefficient of drag (C_A) value is slightly lower than that of the 70° sphere-cone forebody [25]. Additionally, the forebody's dominance has a slight effect on the overall CA.

Prior to the SR-1 launch mission, pre-flight simulation is necessary to ensure the vehicle performs as expected. The Program to Optimize Simulated Trajectories II (POST2) simulation program is used to characterize the vehicle's behavior in the SR-1 mission. It is a 6-degree-of-freedom flight mechanics simulation program with multivehicle capabilities for trajectory integration in translational and rotational equations of motion, as well as trajectory optimization [23]. Since there are no strong indications of autorotation at different angles of attack or side slip angles, and the rolling rate is expected to remain between 40 and 70 deg/s, [24]. An axisymmetric congruity assumption was included in the simulation due to the lack of SR-1 ground test data for the supersonic regime and stable performance observed during the subsonic ground tests of the subscale SR-1. This assumption allows the simulation to reduce the number of variables by parameterizing the total angle of attack instead of using individual matrices for side slip angle and angle of attack. The results of the nominal pre-flight simulation are presented in figures 12 and 13.
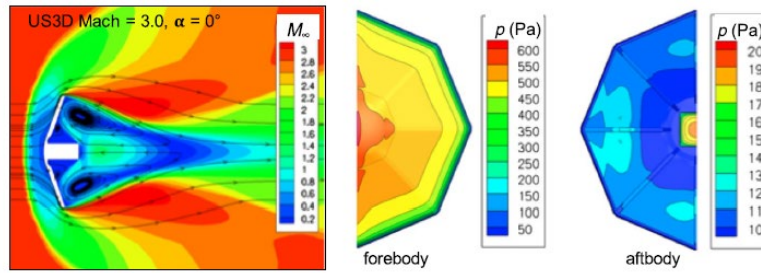
Figure 10. Freestream Mach number contours and forebody surface pressure contours for Mach 3 conditions
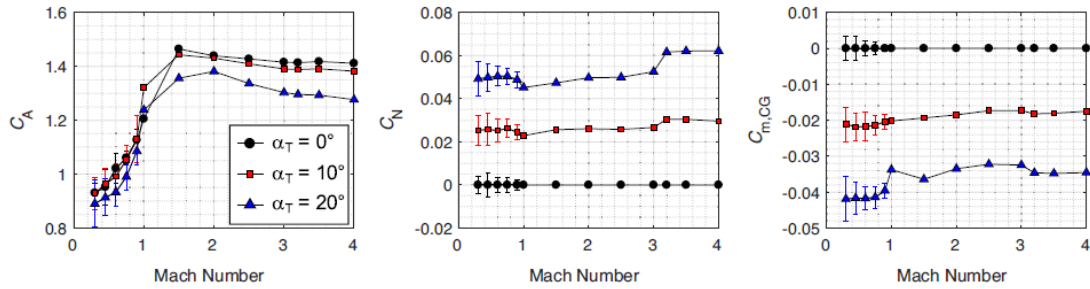
Figure 11. Nominal supersonic continuum static aerodynamic (α_T plane)

1.2.4 SR-1 Flight Result

The SR-1 flight experiment is the first end-to-end test to demonstrate the possibility of the ADEPT for future application with a nano-ADEPT class as a scale down test equipment. Figure 4 shows the operation concept of SR-1, the ADEPT deploys at the altitude of 110 km and marches toward to the ground with no parachutes. It hits its peak Mach number of Mach 3 at altitude of 70 km and strikes the ground with the impact speed of 25 m/s after a 15 min flight.

From the reconstructed flight result, the SR-1 coefficient of normal force C_N, and side force coefficient C_y were under-predicted while yaw moment coefficient C_m and pitch moment coefficient C_n were over predicted. This causes the total angle of attack to oscillate between 0 to 20 degrees before the vehicle reaches Mach 0.5 in figure 12. The sideslip angle and angle of attack shows a sign of affecting the overall result independently, and it may create a larger rolling moment than the simulation selected database. In the meantime, the C_A was underpredicted at Mach 3, and the aft body pressure shows a significant contribution factor for the total C_A which its CFD simulation result error could cause the unpredictability of the pre-flight simulation.
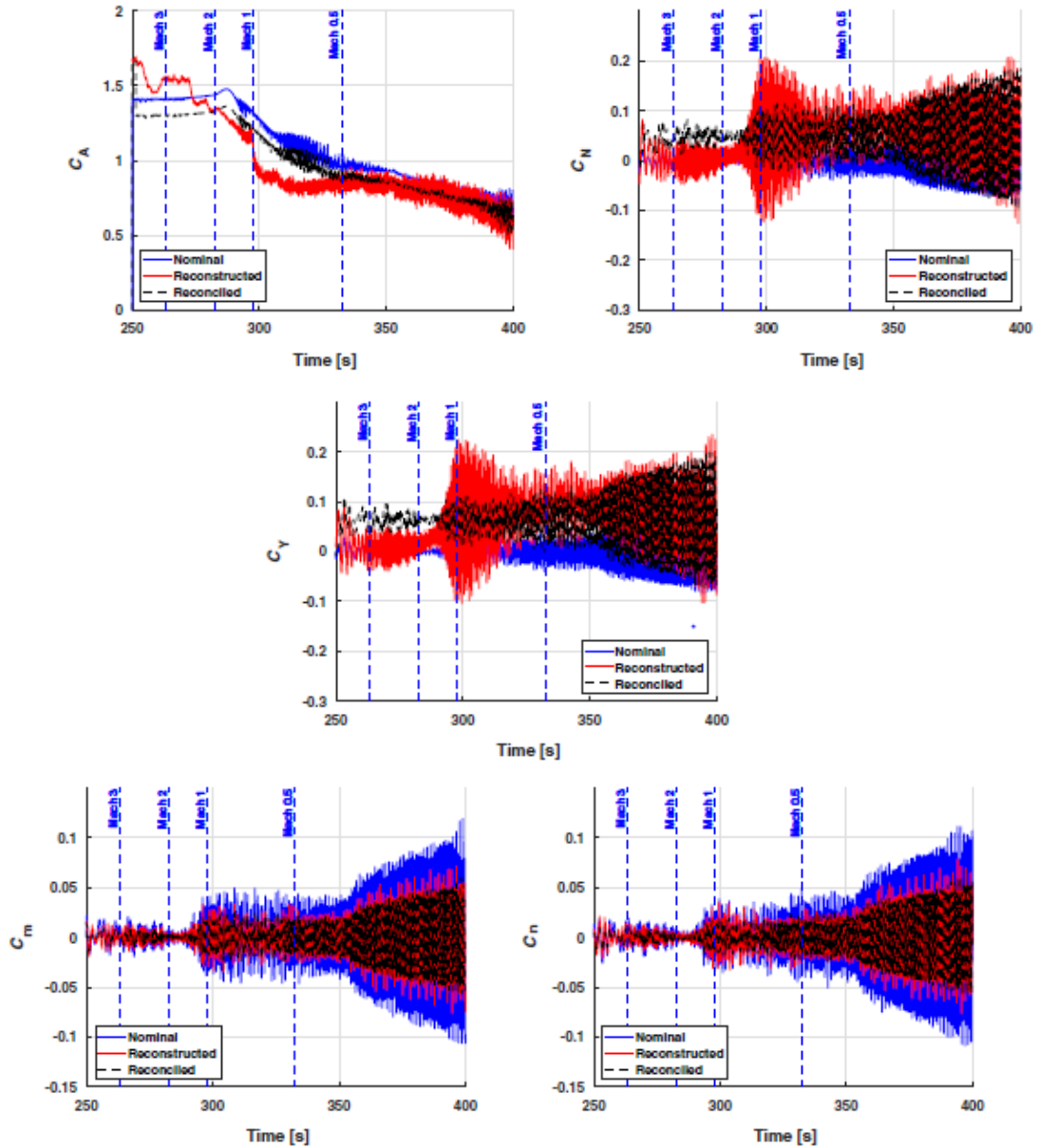
Figure 12. ADEPT SR-1 Comparison between preflight nominal, reconstructed, and reconciled aerodynamic force and moment coefficient [4]

In the meantime, the ADEPT experienced extreme roll angular rate increase after reaching the peak Mach speed as shown in figure 13, and this was not predicted from the preflight simulation. The roll rate between peak Mach and transonic speed was estimated around 40 to 70 deg/s from the preflight simulation but SR-1 roll rate exceeded 218 deg/s when the spacecraft reached Mach 2 during the experiment from the reconstruction data which over 300% difference from the simulation. The reconciliation simulation was created based on the pre-flight data with updated changes such as environment condition on the day of flight and center of gravity adjustment for any possible roll moments changes. The large radial center of gravity due to the faceted shape rib tip was taken into reconciliation consideration where possible shift of the radial center of gravity offset can occur.

9

(a) Total angle of attack   (b) Roll rate
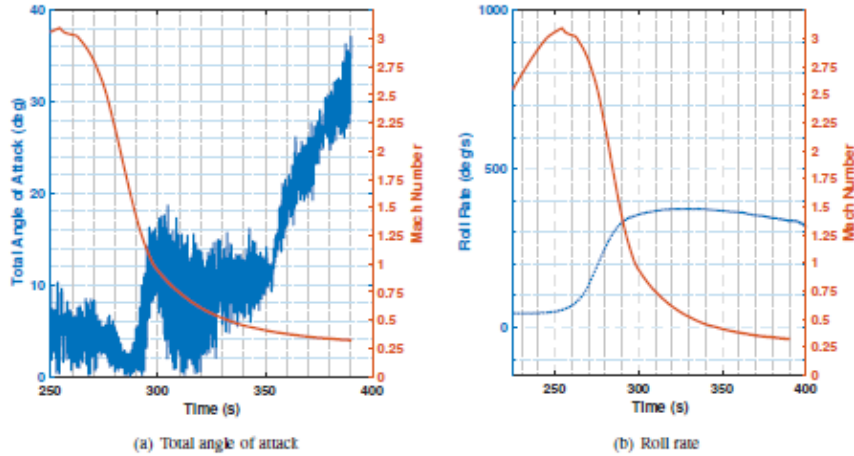
Figure 13. ADEPT reconstructed altitude dynamics profile comparison with Mach number [4]

However, the large roll rate increase was not predicted in the pre-flight simulation nor the reconciliation simulation with changes according to the SR-1 experiment as shown in figure 14. The Mach 3 supersonic condition becomes a critical event and time frame for future SR-1 analyses as vehicle perform unexpectedly than the pre-flight simulation. Korzun et al noted that the angle of attack and sideslip angle each can create moments larger than the original ADEPT ADB where axisymmetric assumption is applied in the preflight simulation [12]. The axisymmetric assumption is that moments created by the slip angle and angle of attack are assumed equivalent in the pre-flight simulation as shown as the nominal data in figure 12. Because of the unique design of the ADEPT, there is not enough data or knowledge to explain the cause of this phenomenon since most of the entry technologies are blunt bodies with axisymmetric shape. The pre-flight simulation axisymmetric assumption related to total angle of attack and faceted shape related data in supersonic condition are the two main focus for the future ADEPT investigation [4]. These flight measures can be an uncertainty factor for estimation of the flow field encountered by the heat shield during entry which means the geometry design or the trajectory of the aeroshell can be critical for the survivability of the vehicle [5].

Figure 14. Roll rate comparison between prediction and reconstructed values

10

1.3 Project Objective

The objective of this project is to investigate the aerodynamic phenomenon of ADEPT during SR-1 experiments and identify the possibility of ADEPT pre-flight simulation axisymmetric assumption error. The result of this report 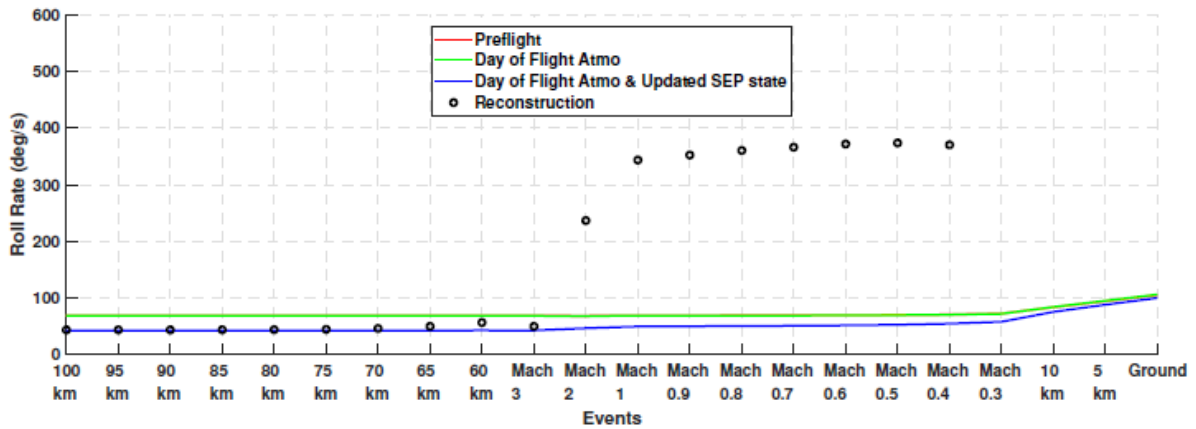will be carried out by the ANSYS Fluent CFD module. Specifically, ADEPT models will be compared in CFD simulations to assess whether axisymmetric modeling contributes to the underprediction of moments and spin rates experienced during flight.

1.3.1 Methodology

This project aims to achieve its results using the ANSYS Fluent CFD module in conjunction with Computer Assisted Design software Solidworks to collect data from a similar flight environment. The SR-1 geometry, provided by the ADEPT program of NASA, will serve as the basis for the simulation settings, which will be adjusted accordingly based on the SR-1 model results. The forebody model will be simulated under specific conditions to recreate a realistic SR-1 experiment environment during reentry, particularly between Mach 3, where the unusual roll rate occurs.

The analysis will be divided into three parts. Initially, the SR-1 model CFD simulation will be conducted using the 2D axisymmetric setting to create a more accurate CFD model. The 2D axisymmetric models will be used to validate the 3D model and simulation settings by comparing them with NASA's simulation data, serving as the baseline criteria. Once the initial criteria are met and the 2D axisymmetric models provide a reliable baseline, the same simulation settings will be applied to the next phase involving steady-state simulation on 3D faceted and 3D axisymmetric rotated model (rotate model). In the meantime, the 2D axisymmetric simulation will attempt to recreate similar SR-1 performance from its flight experiment result to confirm the axisymmetric assumption error. However, 2D axisymmetric simulation can only be done on 0° AOA due to AOA specific flow cannot be simulated in an axisymmetric flow field which 3D rotated model is required. Simulations with 3D faceted models with different roll angles and 3D rotated model will be performed and compared with similar environment condition and setting to study the flow reaction on the shield in Mach 3. Any possible aerodynamic differences between the SR-1 geometry and 3D axisymmetric rotated geometry can be found in the simulation result if it is caused by the forebody. Through these simulations, valuable insights into the aerodynamic behavior of SR-1 during its reentry phase, especially with regards to its unusual roll rate and unique geometry, will be gained.

1.3.2 Assumption and Constrains

The project's geometry will be based on the original test subject SR-1, featuring a simplified aft body and a more detailed forebody to investigate the unanticipated roll moment and characterize the aerodynamic performance. The detailed geometry of the SR-1 can be reviewed in figure 7, with rib parameters subject to adjustments based on simulation and SR-1 flight test results.

The SR-1 roll rate begins to accelerate after it reach the peak Mach which marks this as crucial event of the experiment. The CFD simulation will focus on the period where SR-1 reaches its peak Mach period which at the speed of Mach 3 in table 1. The project's environmental assumptions and constraints will be based on the SR-1 experiment conditions such as altitude and dynamic pressure, allowing for meaningful result comparisons and serving as a reference for future models.

Table.1 Trajectory condition as key test events

Event	Time from launch, s	Altitude, m	Mach	Dynamic pressure, Pa	Angle of attack, deg
ADEPT SR-1 separation	96.31	93,240	2.2267	0.1825	170.7872
ADEPT SR-1 deploy	134.7	107,760	0.8429	0.0016	−171.7977
Apogee	156.18	109,930	0.4421	0.00030829	99.6279
ADEPT SR-1 reentry	229	84,945	2.655	1.3248	15.8879
Peak Mach	254.37	64,602	3.0954	66.483	−2.473
Peak dynamic pressure	281.9	40,871	2.0536	818.4003	−0.493
Mach 0.8	306.63	31,454	0.8	473.9746	−10.9537

1.3.3 Test Models

The 2D axisymmetric models are used to create directed comparison with SR-1 result to identify the axisymmetric assumption error and used a baseline model setting for future simulation. The testing models will consider various angles of attack and roll angles in their CFD simulations to account for the non-axisymmetric characteristics of the SR-1 vehicle. Each individual 2D axisymmetric model meshes consisted of different roll angles to identify aerodynamic difference between roll angles in SR-1. The range of roll angles to be tested is from 0° to 22.5° aligned with rib-to-rib angles of 45° from figure 15. For each individual roll angle, a 2D axisymmetric mesh will be generated with the same flow field dimensions. Additionally, the baseline simulation will include a 3D faceted model and a 3D rotated model with a 0° roll angle, as specified in Table 2. All simulations will be performed at 0° AOA and Mach 3 condition, representing the peak Mach phase of SR-1's flight.

The range of roll angles for the 3D faceted models will correspond to the series tested in the 2D axisymmetric models, while the 3D rotated model with a 0° roll angle will also be selected to align with the axisymmetric assumption due to the absence of z-direction flow in the 2D axisymmetric simulation. Furthermore, transient simulation will be used to observe the vehicle's aerodynamic stability with additional time dependency, which cannot be captured in the steady-state simulation. The transient simulation will focus on an angle of attack of 2.3°, corresponding to the AOA at which SR-1 experienced its peak Mach during the SR-1 flight experiments key event in Table 3 [5].
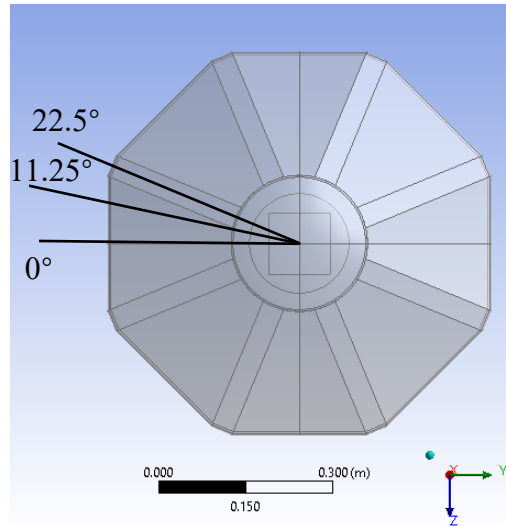
Figure 15. Model roll angle distribution

Table.2 list of 2D test models

Simulation #	2D / 3D	Roll angle	Mach
# 1	2D	0°	3
# 2	2D	11.25°	3
# 3	2D	22.5°	3
3D faceted	3D	0°	3
3D rotated	3D	0°	3

Table.3 List of 3D test models

Simulation #	3D Faceted / 3D Rotated	AOA	Encounter angle / roll angle
A1	3D Faceted	0°	-
A2	3D Rotated	0°	0°
B1	3D Rotated	5°	0°
B2	3D Faceted	5°	6°
B3	3D Faceted	5°	11.25°
B4	3D Faceted	5°	16°
B5	3D Faceted	5°	22.5°
B6	3D Rotated	5°	0°
C1	3D Faceted	10°	0°
C2	3D Faceted	10°	6°
C3	3D Faceted	10°	11.25°
C4	3D Faceted	10°	16°
C5	3D Faceted	10°	22.5°
C6	3D Rotated	10°	-
D1	3D Faceted	15°	0°
D2	3D Faceted	15°	6°
D3	3D Faceted	15°	11.25°
D4	3D Faceted	15°	16°
D5	3D Faceted	15°	22.5°
D6	3D Rotated	15°	0°

13

2. Simulation Set Up

The test models will be considered as axisymmetric and 3D models, with speed, angle of attack, and side slip angles as testing variables, as shown in Table 2. The symmetric model simulations are created to better understand the flow and encounter different angles of attack and roll angles in the geometry.

2.1 General

The selection of the density-based solver is based on its high-speed stability compared to the pressure-based solver. As the mission involves high-altitude environments and the entry stage, gas compressibility must be considered. The pressure-based solver becomes unstable beyond Mach 0.3, leading to increased computational power and time requirements due to smaller time steps for energy and turbulence model calculations. In contrast, the density-based solver was designed specifically for high-speed compressible flow, determining pressure from the equation of state without solving pressure correction equations. Hence, it was the preferred choice for this simulation. Both steady and transient time solutions will be employed to understand how the aeroshell's geometry influences the flow field at instantaneous moments and steady stages. However, the transient time solution will receive greater focus due to the significance of capturing time-accurate phenomena.

The energy equation model was chosen for all simulations as it enables the incorporation of energy or heat transfer functions within the model and couples the velocity with static temperature for compressible flow. This is a requirement in Fluent for ideal gas incorporation.

The Density-Based Solver offers both implicit and explicit coupled methods. The implicit method, chosen for this simulation, provides greater efficiency and larger time scales for the main flow perturbations while still delivering accurate results, especially for large flow fields. The Advection Upstream Splitting Method (ASUM) was selected as the numerical flux function for this simulation.

For this simulation, the flow characteristics correspond to the altitude of the flight trajectory depicted in Table 4, specifically when the spacecraft reaches its peak Mach condition. Assuming a standard atmosphere, the initial condition of the free stream is given in Table 1. These choices were made to ensure the simulation accurately represents the real-world conditions during the SR-1 mission.

Table 4. Initial free stream conditions corresponding to 64km altitude

Altitude (km)	64
Mach Number	3
Free stream Velocity (m/s)	960
Free stream Temperature (K)	254.6
Free stream Density (kg/m3)	0.000683
Dynamic Viscosity (Pa-s)	0.000017234
Free stream Pressure (Pa)	50

The ANSYS Fluent offers a range of turbulence models based on the Reynold-averaged Navier-Stokes equation, as represented in Eq. (1). Due to the averaging procedure in the RANS momentum equations, the presence of the Reynold Stress term introduces additional unknowns, necessitating modeling to close the system of state equations. One popular approach is the eddy viscosity model, which employs the Boussinesq hypothesis to relate the Reynold stress to an eddy viscosity.

$$\rho \bar{u}_j \frac{\partial \bar{u}_i}{\partial x_j} = \rho \bar{f}_i + \frac{\partial}{\partial x_j} \left[-\bar{p}\delta_{ij} + 2\mu \bar{S}_{ij} - \overline{\rho u'_i u'_j} \right].$$

(2.1)

For this specific project, the one equation Spalart-Allamaras (SA) turbulence model is selected as the turbulence model due to its numerical robustness and simplicity, making it well-suited for the analysis of the forebody. The SA model is based on the RANS equations and has demonstrated stable performance, allowing for reduced computational costs and faster convergence of CFD solutions. NASA's US3D simulation for the SR-1 preflight test in the supersonic regime also successfully utilized the SA model. The governing equations are discretized using the finite volume approach. In this simulation, second-order accurate viscous fluxes and turbulent source terms are employed, along with a least squares cell-based gradient approach to obtain a steady solution. A no-slip wall condition is applied at the boundaries. The flow properties are set to represent calorically perfect air, and the viscosity is modeled using Sutherland's law, following the ADEPT SR-1 preflight simulation [2].

2.2   Model Mesh Setup

There are three types of models meshes being used in this simulation: the original 3D SR-1 faceted model, 2D axisymmetric model, and 3D rotated model, depending on different roll angles. As shown in figure 16, the SR-1 2D axisymmetric is created by a slice of a selected roll angle of the SR-1 model, and 3D rotated model is a revolved SR-1 slice with certain roll angled according to Table 2 and 3. The difference between the 2D axisymmetric model and 3D rotated model is z-direction force or moment is included in the 3D model where 2D model does not consider.
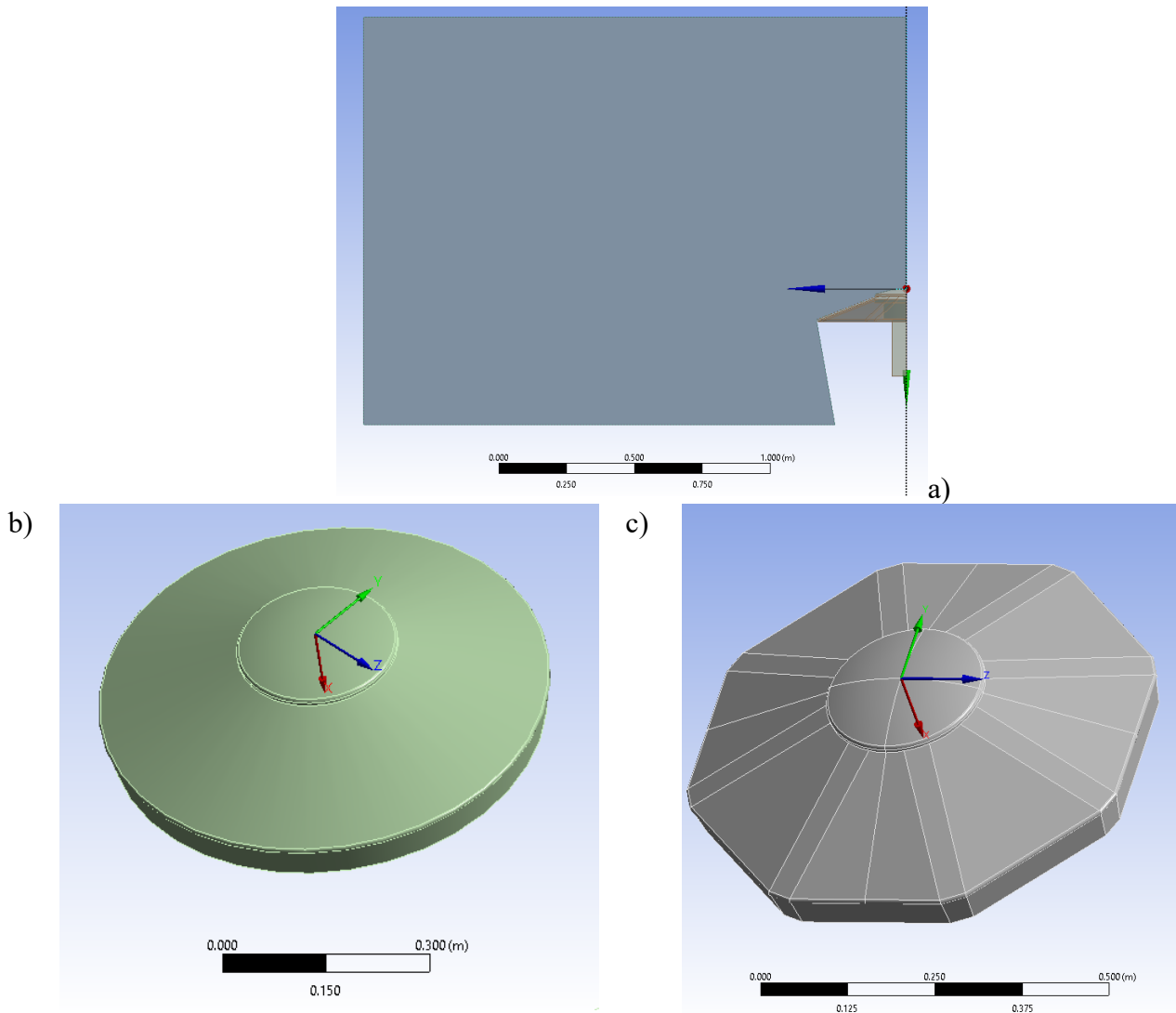

Figure 16. Model overview
a)   2D axisymmetric model; b) 3D rotated axisymmetric model c) 3D faceted model

16

Each 2D axisymmetric model is assigned and created according to the roll angles listed in Table 2. The top tip of the vehicle is located at the global origin, pointing towards the flow field entry as shown in figure 17. A fake aft body connects to the edge of the model and is surrounded by the pressure far field or outlet (shown in yellow). This extra feature does not affect the forebody's results but allows for a stable convergence process during simulation testing. In the 2D model, as shown in figure 17, the flow will enter the pressure far field (shown in blue) by moving towards the positive x-axis direction and exit out of the flow field when it passes the SR-1. The axis is placed at the center of the SR-1 as an axisymmetric axis (shown in red) for the software.
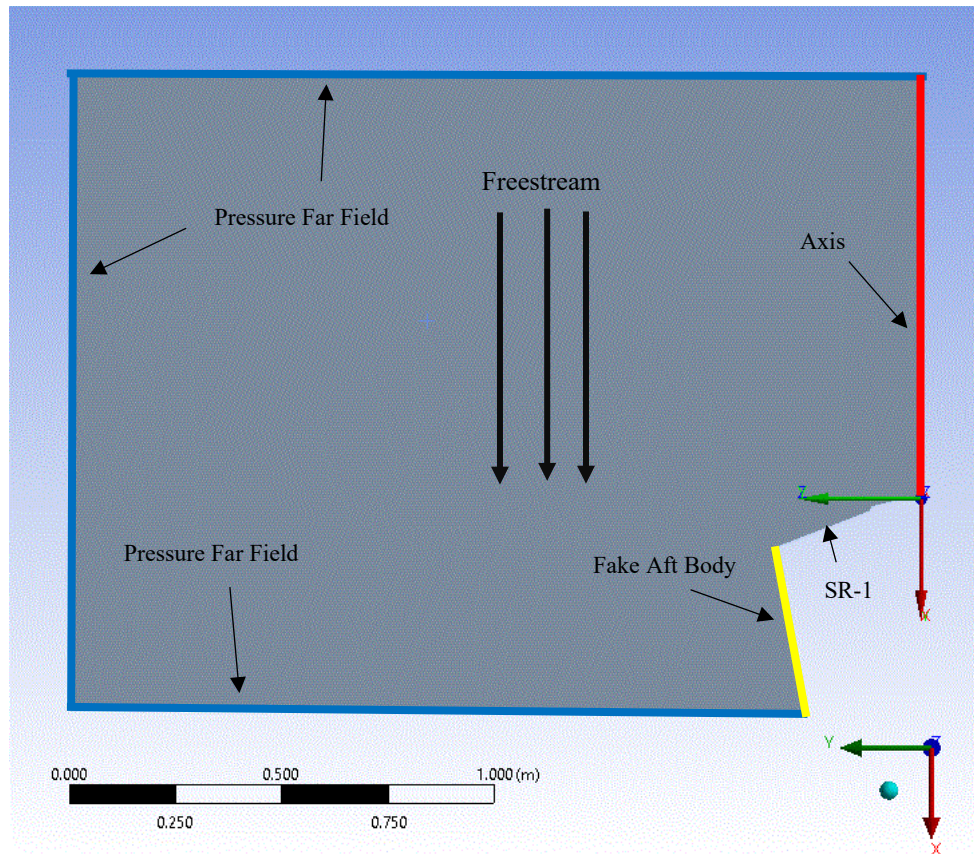

Figure 17. 2D model boundary condition

As for the 3D faceted and rotated model in figure 18, the model is placed in the center of the flow field as well as point toward the negative x-direction. The flow will come in from the inlet (shown in blue) with a specific direction vector to simulate different angles of attack (AOA) and exit out of the outlet boundary or its pressure far field (shown in red). To simulate the AOA, only the axial and normal forces are used in this simulation to avoid data deviations in the side force and roll moment calculations caused by angled flow. Since the unique SR-1 octagon-shaped shield has different radii with different roll angles, each roll angle between ribs should be simulated to ensure aerodynamic effect difference caused by the different radii can be observed in this simulation.

For each roll angle, the model mesh will rotate accordingly before each simulation to allow different shield radii to directly encounter the free stream flow. To simplify the data procession, the z direction force should be remained at zero since no side force is included other than axial force and normal force in this simulation. In this simulation, regional meshing methods are employed to streamline the meshing process and reduce the required computational power in the CFD simulations. For both the 2D axisymmetric and 3D mesh models, regions were named accordingly in figure 20 and 21, with different cell sizes listed in Tables 5 and 6. Additionally, surface meshes are applied to the 3D mesh to enhance the simulation's accuracy.
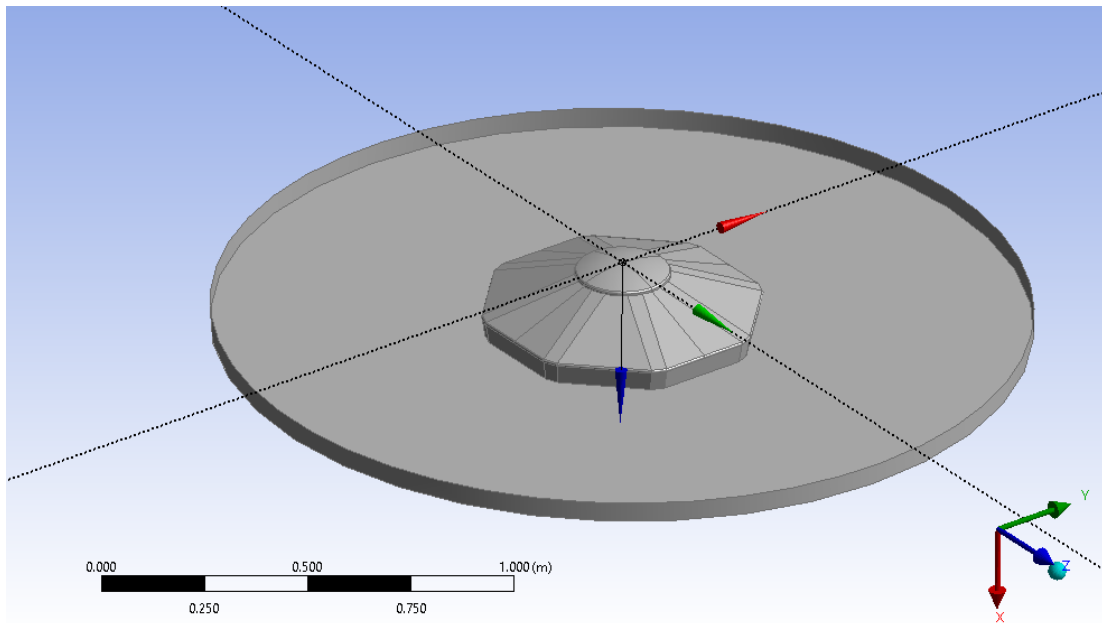
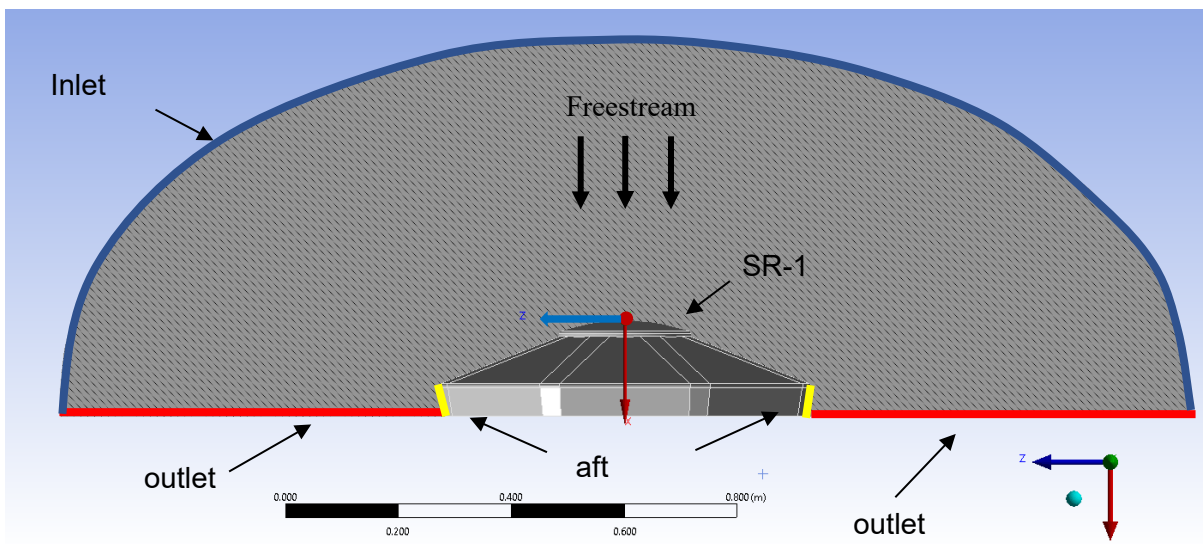

Figure 18. 3D Model overview
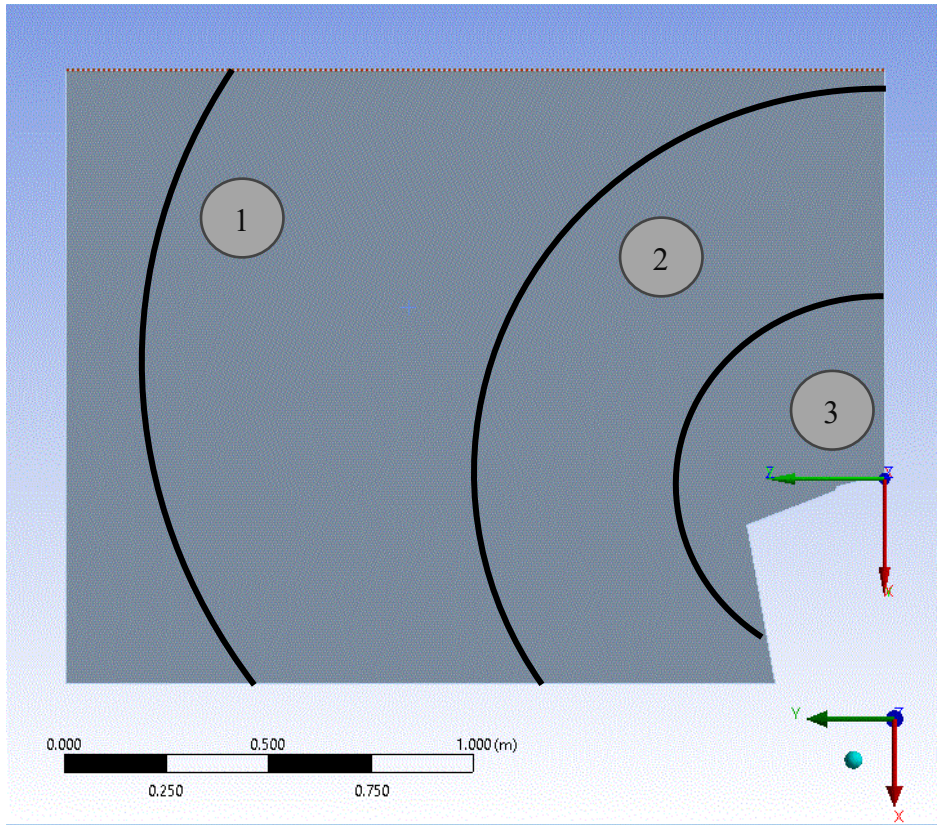

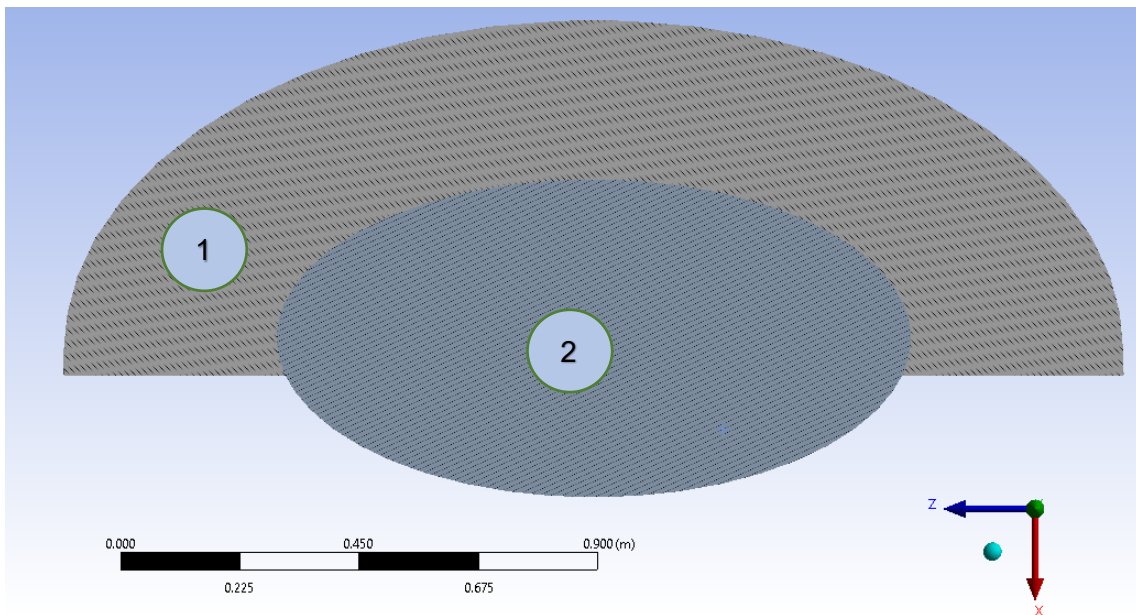Figure 19. 3D model boundary condition

Figure 20. 2D Model mesh region

Figure 21. 3D Model Volume Mesh Region

The choice of mesh model depends on several factors, including accuracy, cell count, convergence rate, overall memory usage, and required time per iteration. For this project, the tetrahedron mesher is selected for both mesh regions due to the complex curvature between the cap and the shield, where only one method is allowed in a single body in Fluent. The tetrahedron mesh provides stability and accuracy in regions with complex curvature, especially around the cap curvature and shield edge, where other methods may result in a high number of low-quality cells. Although the tetrahedron mesh may increase the cell count, it significantly improves the accuracy of the model simulation, especially for complex geometries. Surface meshing is applied to create triangular faces and vertices on the model, resulting in a better-structured face mesh for the incoming volume mesh process. This function allows the model to re-triangulate any poor-quality surface mesh and optimize it for building a more efficient nearby volume mesh. It is particularly beneficial for the 3D faceted model surface and 2D model, ensuring higher accuracy and a consistent grid surface throughout the simulation.

Before implementing the 2D axisymmetric mesh in the simulation, a mesh refinement process was undertaken to verify grid convergence (i.e., ensure the mesh design does not significantly affect results) and enhance efficiency by selecting the appropriate size mesh. The mesh settings used for the 2D axisymmetric model will also be applied to the 3D model mesh. Table 5 outlines the various mesh sizes and combinations considered during the selection process for this project. To account for computational power limitations, simplified SR-1 simulations were conducted using different mesh sizes and settings. Figure 22 shows a short simulation result comparison between ideal meshes size and mesh combination. For mesh selection, the mesh converges is the priority factor for simulation. From the result, the medium and fine mesh combination shows a more stable and converged result compared to the 0.01m and 0.05 m mesh result especially in the gap area between the cap and shield shown in figure 22b. At the same time, computational power is a cortical limitation with 0.005m size mesh required a significant amount of computational power more than medium and fine mesh combination in simulation. Ultimately, the medium mesh combination was chosen for its optimal balance between computational efficiency and validity, and the final mesh product shown in figure 23.

Table 5. 2D Axisymmetric Mesh Generation Parameter

|	Uniform Mesh Size			Mesh Combination		
	0.05 m	0.01 m	0.005 m	Coarse (Simple)	Medium	Fine
Region 1	0.05 m	0.01 m	0.005 m	0.02 m	0.01 m	0.005 m
Region 2	0.05 m	0.01 m	0.005 m	0.008 m	0.004 m	0.002 m
Region 3	0.05 m	0.01 m	0.005 m	0.004 m	0.002 m	0.001 m
Tager skewness	0.9	0.9	0.9	0.9	0.9	0.9
Element Quality	0.97171	0.9685	0.96069	0.97073	0.96462	0.93642
Aspect Ratio	1.1709	1.1791	1.2073	1.1717	1.1933	1.2929
Skewness	0.042476	0.047435	0.05912	0.044011	0.053248	0.096778
Orthogonal Quality	0.97379	0.97078	0.96344	0.9729	0.96718	0.94043

a)

b)
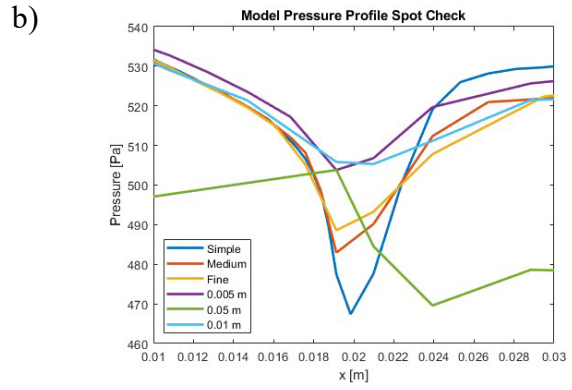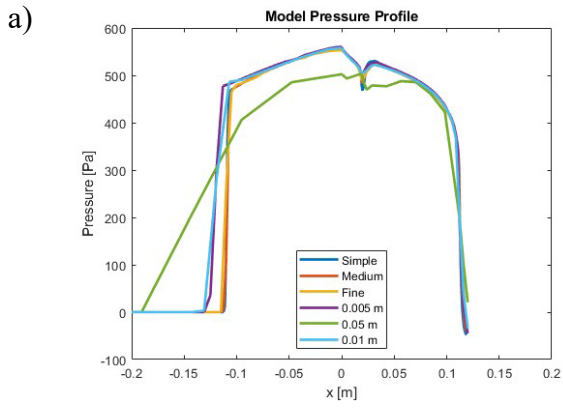
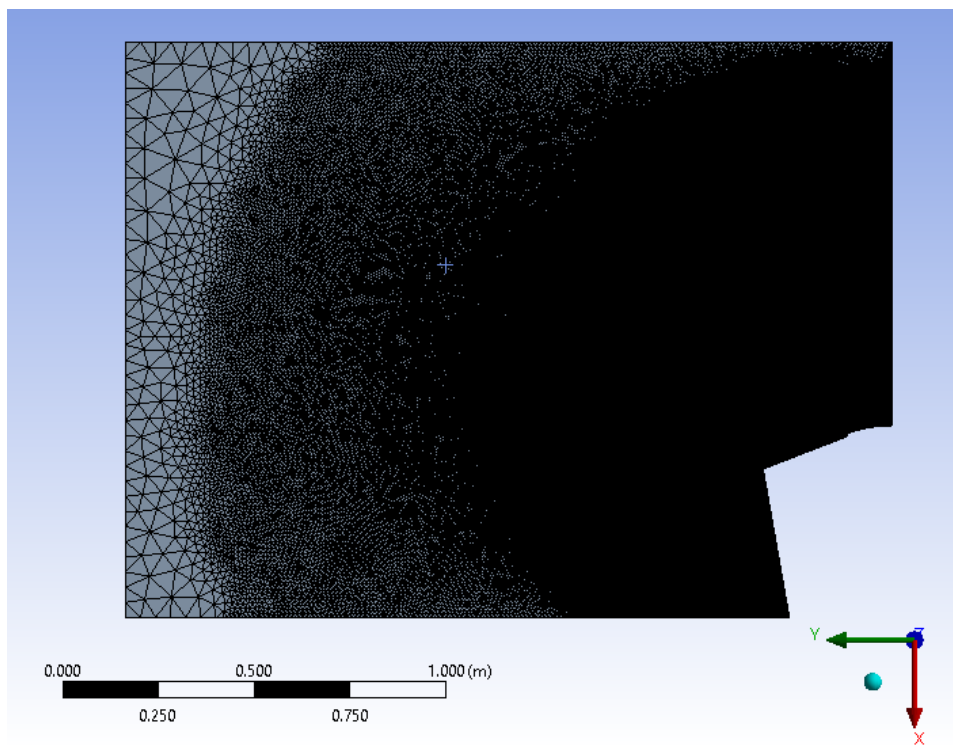Figure 22. 2D model mesh selection result

Figure 23. 2D model mesh overview

Parameters used for 3D faceted mesh generation are shown in Table 6. The outcome of applying these parameters generated a mesh that had 3,768,976 tetrahedral cells, 7,604,422 interior faces, and 665,733 vertices. The mesh overview is shown in Figure 24.

Table 6. Parameter Used for Final 3D Mesh Generation

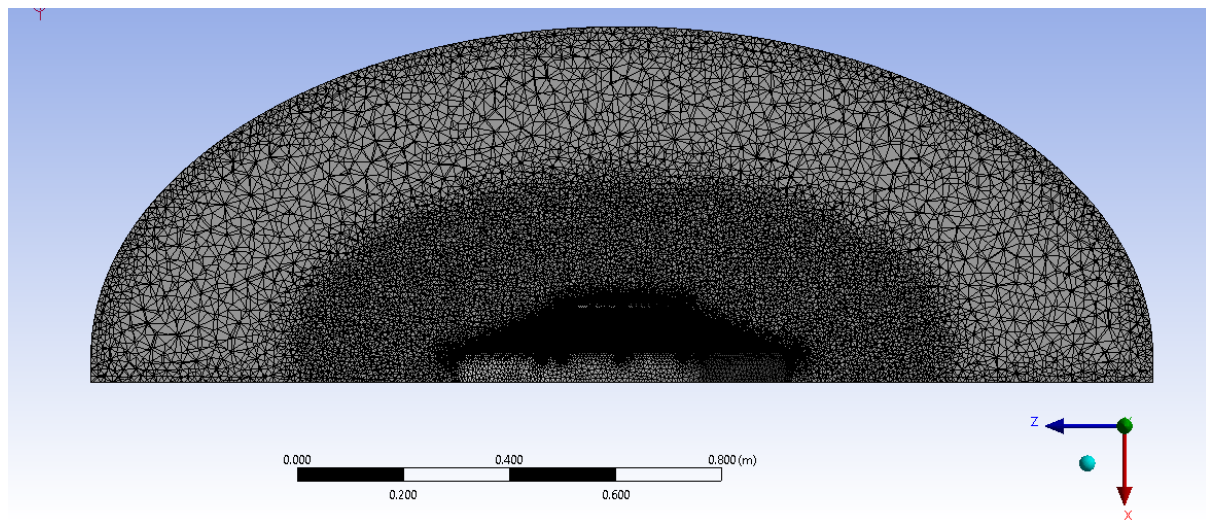| Region 1	
Target Size (m)	0.015
Growth Rate	1.2
Max Size	0.003
Target Skewness	0.9
Region 2	
Base Size (m)	0.01
Growth Rate	1.2
Forebody Surface	
Base Size	0.005
Growth Rate	1.2

Figure 24. 3D model mesh size view

3. Test Result
3.1 2D test result

The objective of the 2D axisymmetric test is to establish reliable simulation settings for future simulations, aligning them with NASA's results. The adjustment of simulation settings will be based on comparing the outcomes obtained from this 2D axisymmetric simulation with NASA's results. By achieving a similar simulation outcome to NASA's, this simulation gains more reliability, minimizing the risk of potential errors.

NASA provided a series of simulation results as the baseline of this project simulation including pressure contour at 0° AOA as shown in figure 25b, and simulation result of different AOA in Table 7. The 2D axisymmetric model pressure distribution of the shield shows similarities in figures 25 which provide confidence of the 2D axisymmetric model simulation accuracy as well as simulation setting. Additionally, the accompanying figure 25 illustrates the flow distribution spreading equally throughout the shield, indicating that the flow does not guide to any specific area as a flow stream. This observation first suggests that the rib parameters does not exert any additional force on the front shield by the current result.
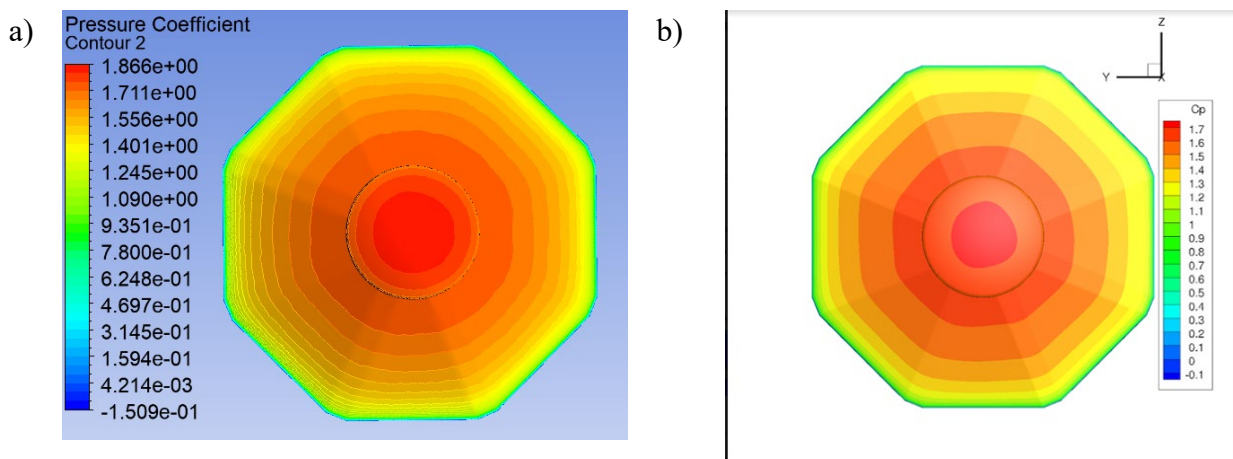

Figure 25. Pressure coefficient contour comparison
a) Simulation pressure coefficient contour
b) NASA pressure coefficient contour [21]

The calculation of SR-1 coefficient results is based on the forces acting along specified vectors and the moments around a designated center along a specific axis of the SR-1 section wall. The total force of SR-1 is obtained by summing the dot products of the pressure and viscous forces on each face of the wall with the specified force vector. The force coefficient is defined as the sum of the total force and the dot product of the viscous force, divided by the reference value of $\frac{1}{2}\rho v_f^2 A$, where ρ represents the freestream density, v_f is the freestream velocity, and A is the reference area. To compute the moment about the center of gravity, the cross product of the pressure and viscous force vectors for each face is summed with the moment vector r_{AB}, which represents the vector from the center of gravity A to the reference point B. The moment coefficient is then defined as the total moment sum divided by the moment constant of $\frac{1}{2}\rho v_f^2 AL$, where the reference length is represented by L.

$$\overrightarrow{M_A} = \overrightarrow{r_{AB}} \times \overrightarrow{F_P} + \overrightarrow{r_{AB}} \times \overrightarrow{F_v} \tag{3.1}$$

The 0° AOA baseline data series was chosen for direct comparison with available NASA data and is presented in Table 7. The surface area (SA) of the 2D axisymmetric model varies with different roll angles due to the different rib radius for the respective rib angle, resulting in the model experiencing more force when the SA is higher. The data indicates that the C_A for all three models remained within 5% difference from the NASA result, indicating the forebody facets do not have significant effect on the axial forces. The C_N remained at zero, as there were no normal forces at 0° AOA. This result was expected and provided quantitative confidence in the accuracy of the model and simulation settings. In the meantime, 2D axisymmetric model shows a similar result with less than 2% difference indicate a sign of axisymmetric of any SR-1 roll angle does not affect the overall performance of the forebody. The Ansys provided C_m of 0.442 for all three 2D models considering only one side of the shield as shown in the figure 26b, which required other side for overall moment calculation, and resulted in 0 for overall C_m with approval from raw data calculation.

Table 7. 2D baseline result comparison

	NASA	2D 0° roll angle	2D 11.25° roll angle	2D 22.5° roll angle
0° AOA				
SA	0.3716	0.3860	0.4002	0.4241
C_A	1.4561	1.4072	1.4009	1.4199
C_N	-3.7710e-05	0	0	0
C_m	7.3020e-06	0	0	0

In this 2D simulation, the flow moves from the negative x region to the positive region. As the flow encounters the shield cap of the SR-1 shield located at x = 0 m, a shock wave starts forming between x = -0.12 m to 0 m. Beyond x = 0 m, the pressure profile describes the shield pressure distribution in the Mach 3 flow field, and result extending to the edge of the SR-1 shield at x = 0.12 m.

As depicted in figures 26 and 27, the 22.5° roll angle results in the thickest shock standoff thickness at x = -0.12 m, while 0° roll angle model exhibits the thinnest standoff thickness at x = -0.11 m. The only difference between runs is the model radii. The high standoff distance occurs with the 22.5° roll angle model, representing the rib area of the shield, while the lower standoff distance occurs with the 0° roll angle, representing the shield panel between ribs. Analyzing the model's pressure profile in figure 26, it is evident that all 2D axisymmetric model pressure results are closely similar at 0 degrees of AOA as all model experiencing similar flows, except for the difference in standoff distance. The difference in surface area created by the different roll angles leads to changes in standoff distance and, consequently, received pressure, as shown in Table 7 .
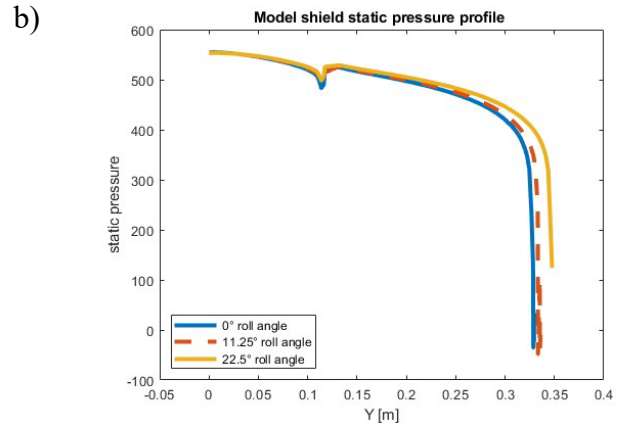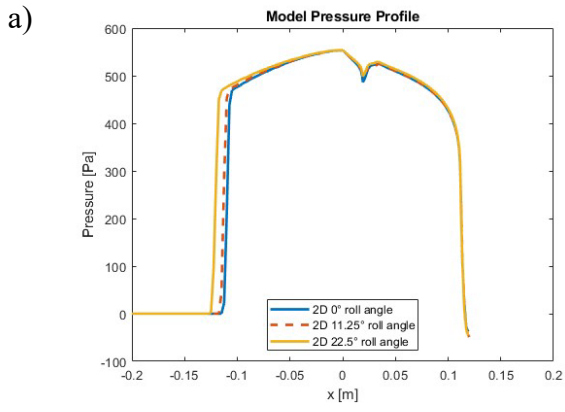
a)

Model Pressure Profile

b)

Model shield static pressure profile

Figure 26. 2D model pressure profile
a) Model pressure profile b) Model Shield Pressure Profile
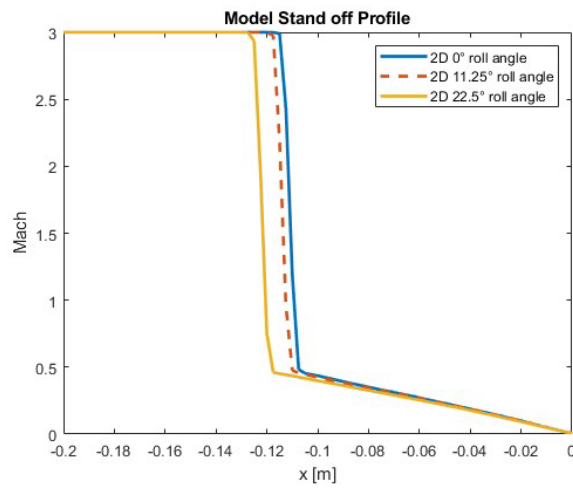
Model Stand off Profile

Figure 27. Model Mach profile comparison

25

3.2 3D Steady test result

The objective of this set of simulations is to characterize the aerodynamics for the 3D faceted geometry in steady-state flow at various angles of attack (AOA) and roll angles. As the simulation starts, the flow enters the flowfield towards the positive x direction and makes contact with the shield at the center of the field. For each AOA, the shock wave forms approximately 0.12m away from its stagnation point, and its subsonic region within the shock wave shifts as the AOA increases, as evident in the contour figures 28 to 29.

Figure 29 presents the pressure coefficient shield contour, where each contour displays the pressure distribution of the shield for each AOA during simulation. As the AOA increases, the high-pressure zone (depicted in red) moves across the shield, and the pressure is evenly spread out from the stagnation point of the shield. This diagram indicates that no unusual pressure regions were detected on the front shield, creating extra force other than the expected axial force and normal force.
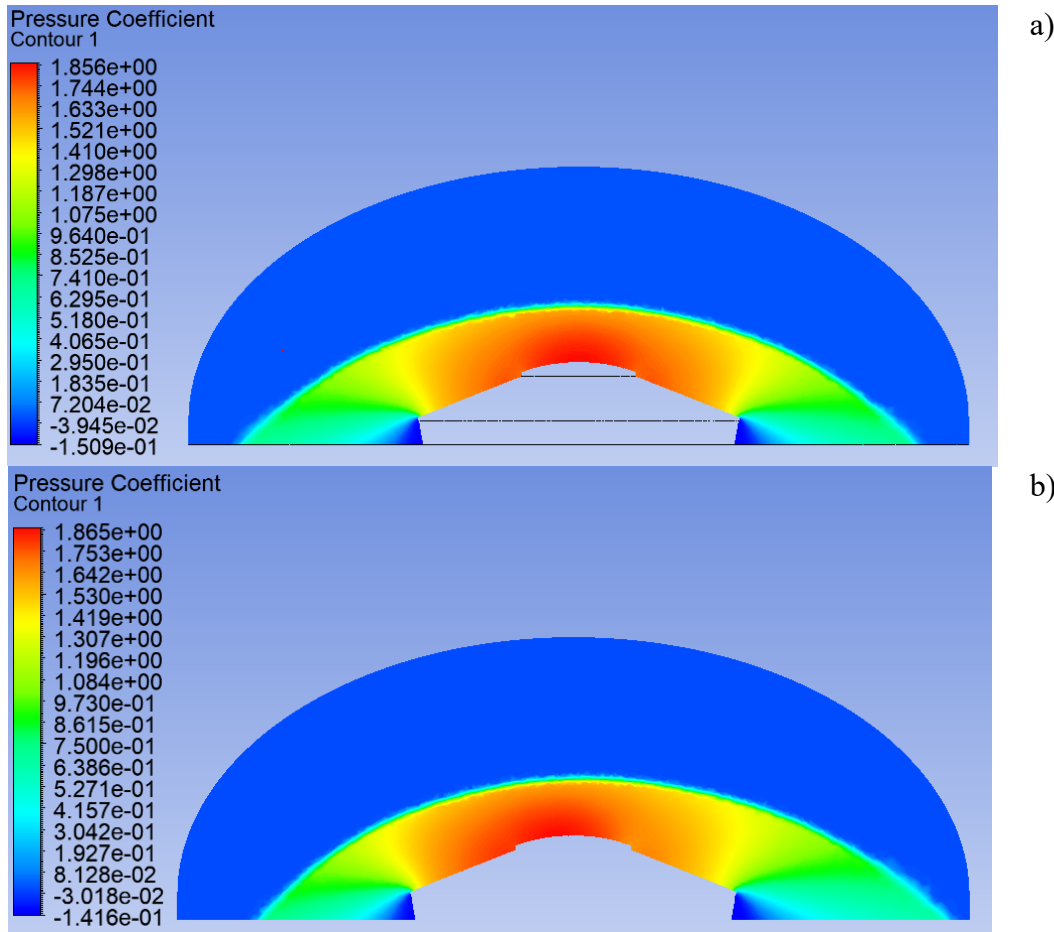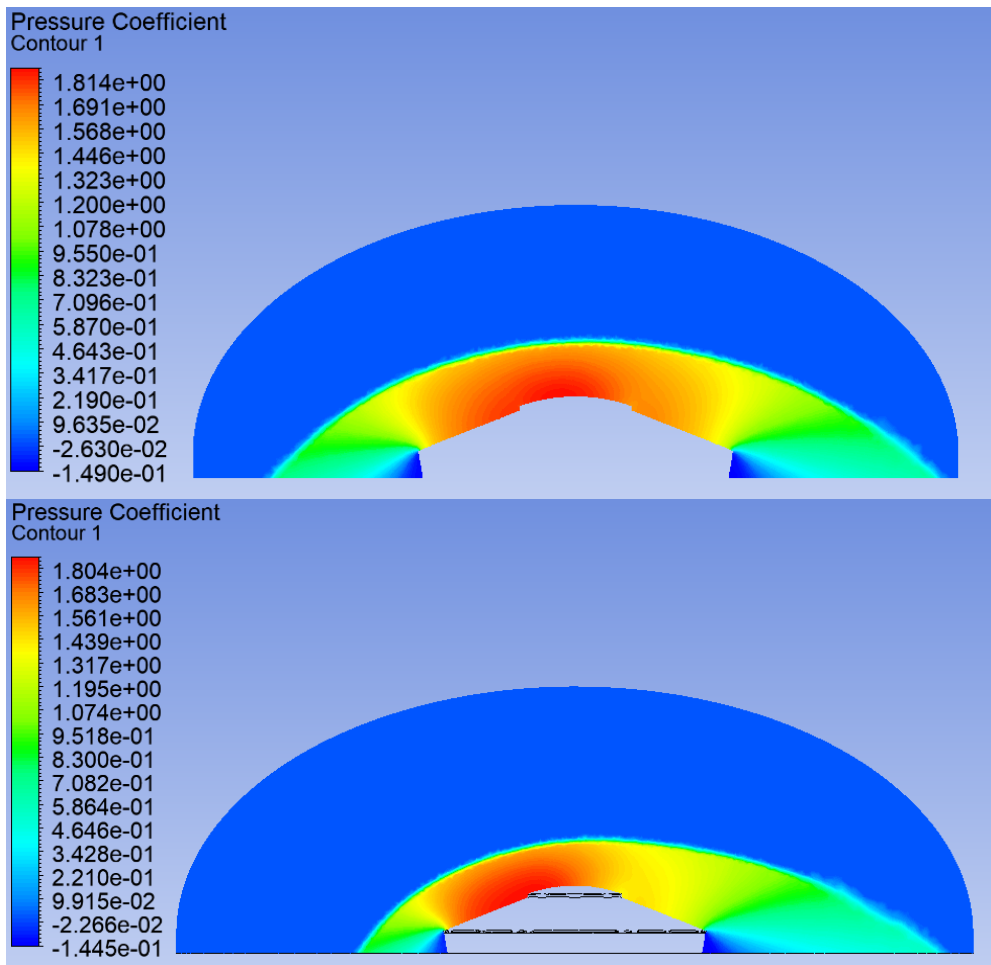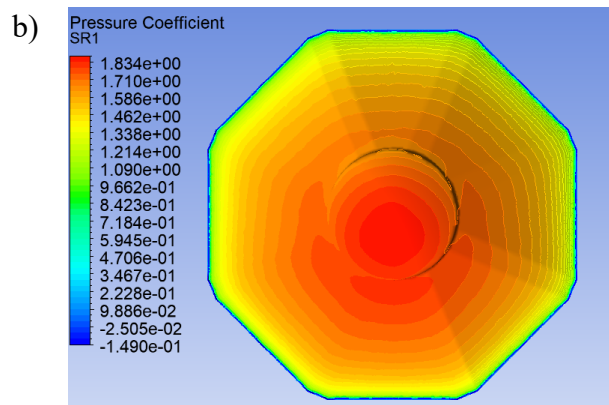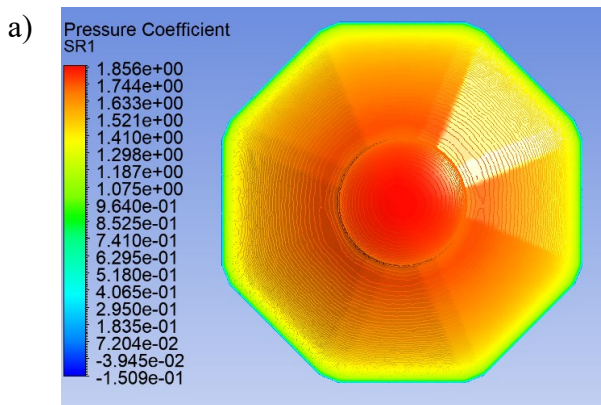
Figure 28. 3D faceted model pressure contour at difference AOA
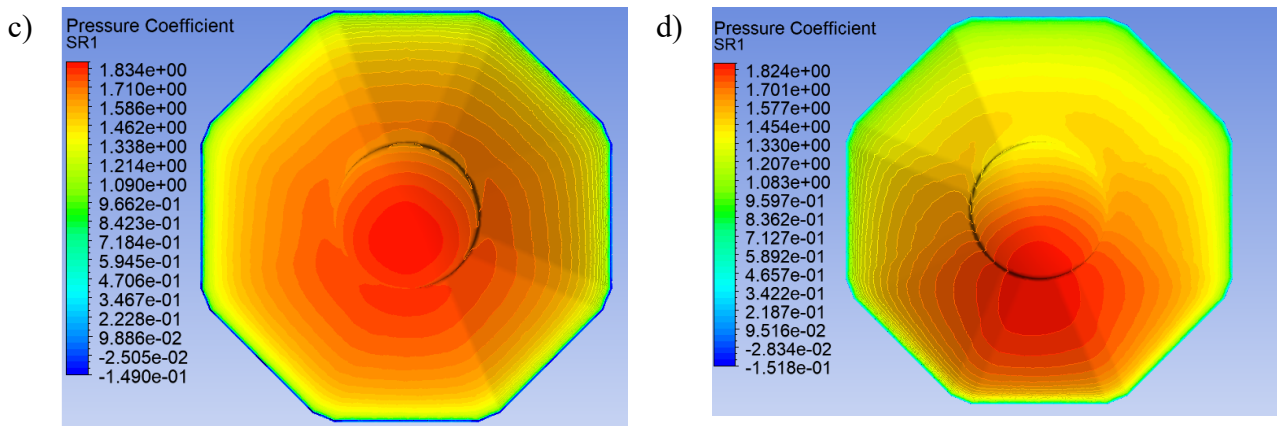a)   0º , b) 5º , c) 10º , d) 15º

Figure 29. 3D faceted model pressure contour on SR-1 shield at difference AOA
a) 0º, b) 5º, c) 10º, d) 15º

As the AOA increases, the axial force decreases, and the normal force increases, confirming the correctness and alignment of the flow direction simulation setup, as anticipated as shown in figure 30. The shield experiences minimal side force in comparison to the axial and normal forces. Specifically, the normal force coefficient ranges between 0 to 0.045 and the axial force ranges between 1.43 to 1.35, while the side force C_y is close to zero.,.

Regarding the moments result, the calculation is performed around the center of gravity with a selected axis, as shown in figure 30. Although the rolling moment exhibits slight signs of increase with rising AOA, the range only amounts to approximately 14×10^{-6}, indicating minimal roll moment created by the front shield in this scenario. The C_m coefficient consistently decreases compared to other moment coefficients, within the range of 0 to -0.035, and this shows a sign vehicle oscillation might occur and leads to higher total angle of attack. The uniformity of the results in figures 30a, 30c, and 30f suggests that different roll angles encountered by the flow have minimal impact on the overall behavior of the vehicle.
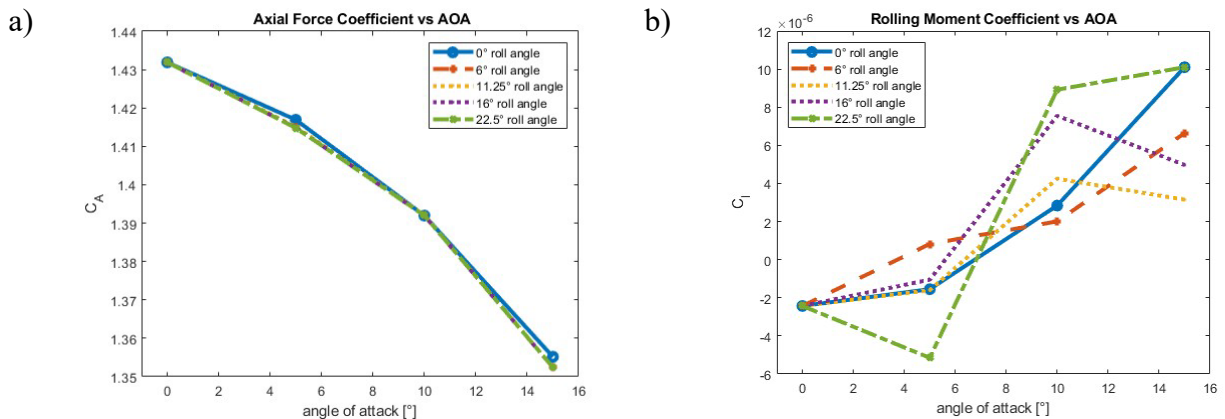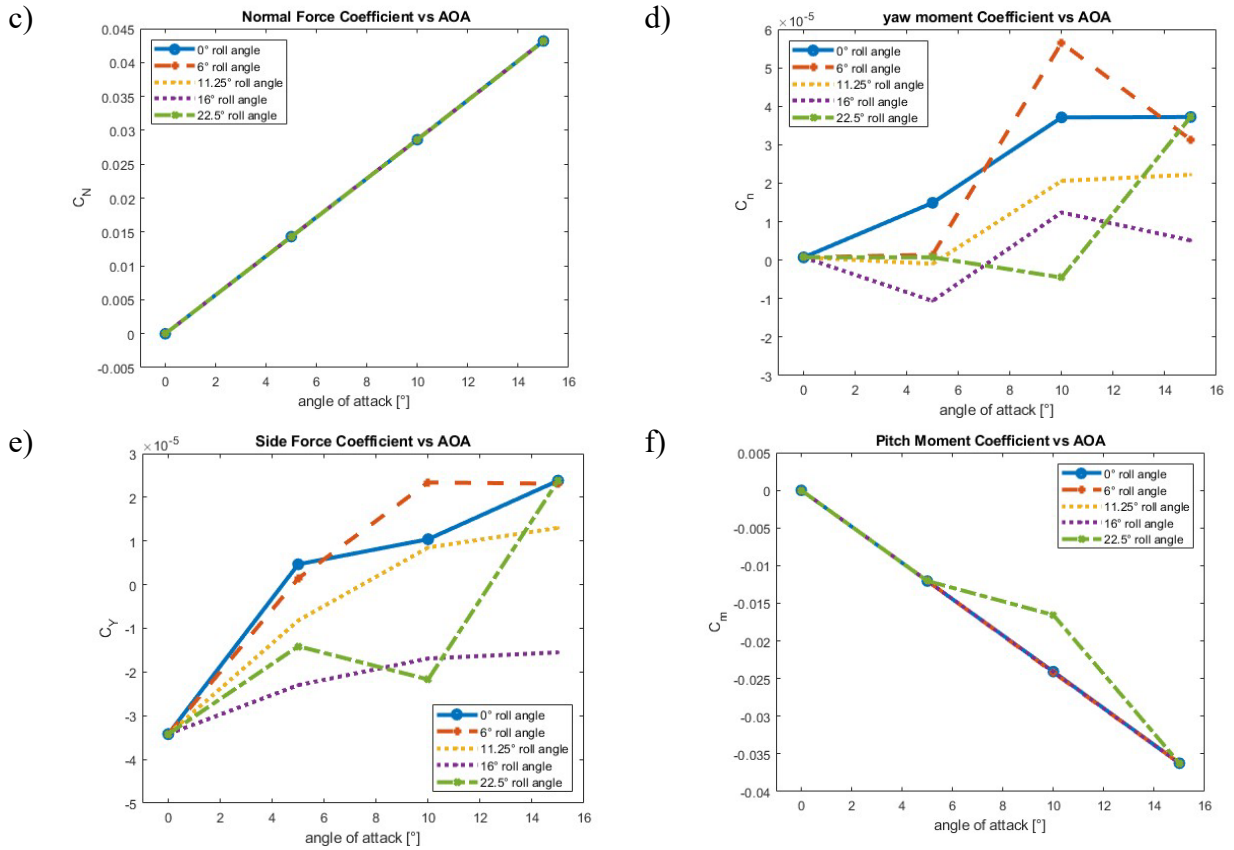
Figure 30. 3D faceted model result as a function of AOA

Figure 31 displays the flow paths for different AOAs. A notable observation is that the 3D faceted model does not exhibit any signs of flow gathers into groups of flow paths, like Figure 9b. The flows remain evenly distributed across the shield, and as the AOA increases, flow starts to gather at the gap area between the cap and the shield, as expected. This indicates that the flow maintains its course when encountering the rib area of the shield. It is essential to note that in CFD, walls are typically assumed to be rigid, which may not fully represent real-world scenarios. The flexibility of the SR-1 material, however, could play a significant role in influencing flow distribution at high speeds.

To further investigate the effect of roll angle and AOA, the center of pressure (CoP) coordinates for each roll angle were collected and depicted in figure 32. The CoP serves as a critical indicator of the shield's stable location under different AOA and provides valuable insights into any unusual forces acting on the shield. The CoP calculation is based on the center of gravity, which is located at x = 0.1032 in Figure 7. The y-axis, z-axis, and center of gravity origin at x = 0.1032 are marked to clarify the SR-1 coordinates. With an increase in AOA, the CoP begins to shift away from the origin, reaching a maximum distance of 0.02m in the y-direction. However, there are minimal changes observed in the z-direction, as the simulation excludes any side forces, resulting in only minor variations in the moment within the range of -1×10^{-5} to 3×10^{-5} m. This indicates that the roll angle does not significantly impact the overall forebody performance of the SR-1 when the flow directly encounters any roll angles.
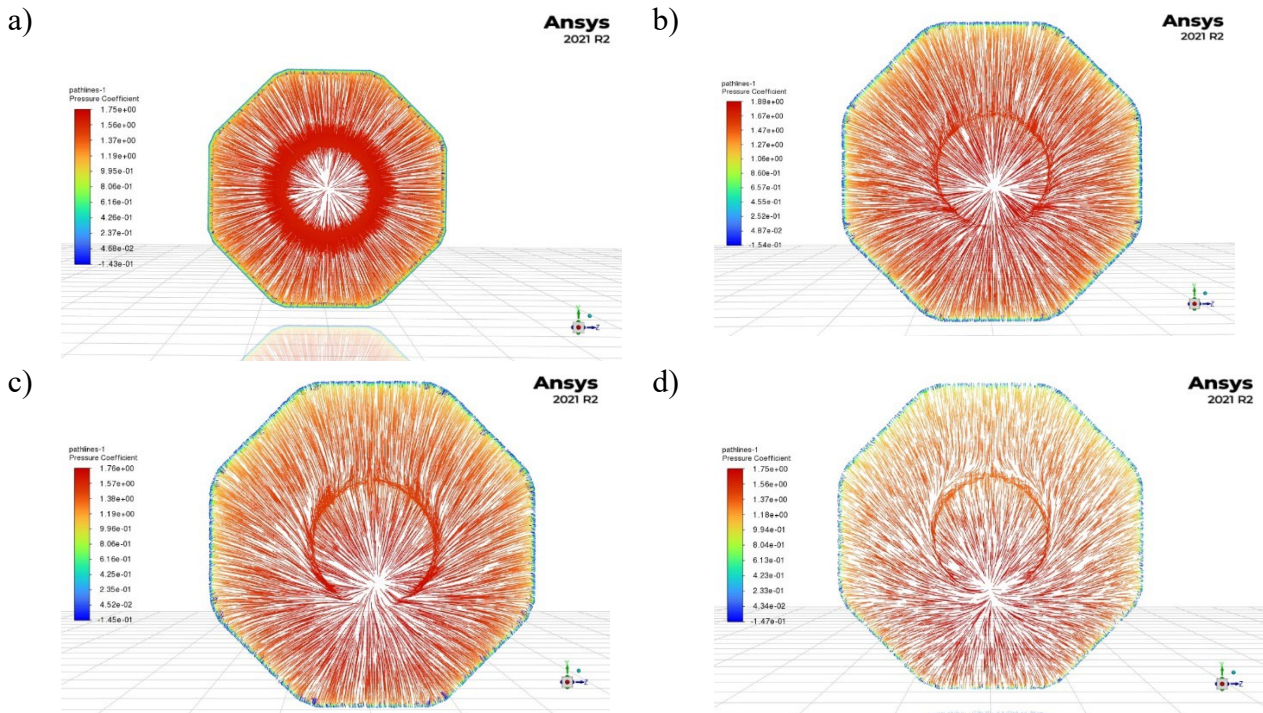
29

Figure 31. 3D faceted model flow path line contour on SR-1 shields at different AOA
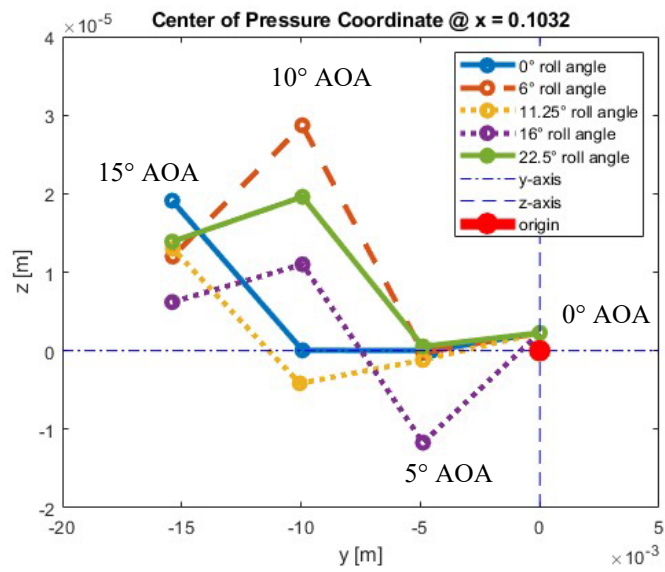0º, b) 5º, c) 10º, d) 15º

Figure 32. Faceted model mapping of center of pressure location as a function of AOA (x = 0.1032)

3.3 3D Rotated Test Result

For the SR-1 preflight simulations, NASA approximated the aerodynamic behavior used an axisymmetric flow assumption. They attributed differences in flight data and preflight simulations to the axisymmetric assumption not sufficiently representing the faceted geometry of the flight vehicle. To test this assertion, a 3D axisymmetric rotated model was created to enable a comparison of the behavior of an axisymmetric flow (which by definition is 2D) in 3D flow to the 3D faceted model. This 3D rotated model for simulation was generated by taking a 22.5° roll angle slice of SR-1 and rotating it around the x-axis to serve as an axisymmetric representation. From section 3.1, the 2D axisymmetric model with different roll angles showed under 5% difference among them, so there was no need to change the forebody radius to represent the other roll angles.

The following figures 33 and 34, represent the 0° AOA pressure profile comparison between the 2D axisymmetric, 3D faceted, and 3D rotated models. The 3D rotated model shows a greater shock standoff distance compared to other models. In the meantime, the 2D axisymmetric model with 22.5° roll angle has a similar standoff as the 3D faceted model while both model shock wave started on x= -0.13m and 3D rotated model started on x= -0.14m. All models experienced similar pressure on the shield according to the shield profile in figure 33.
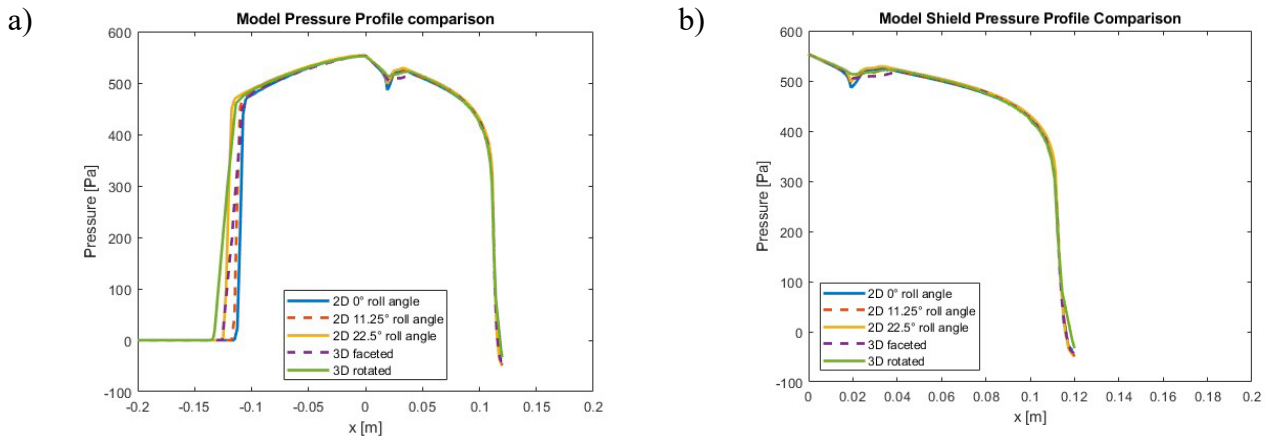

Figure 33. Model pressure profile comparison
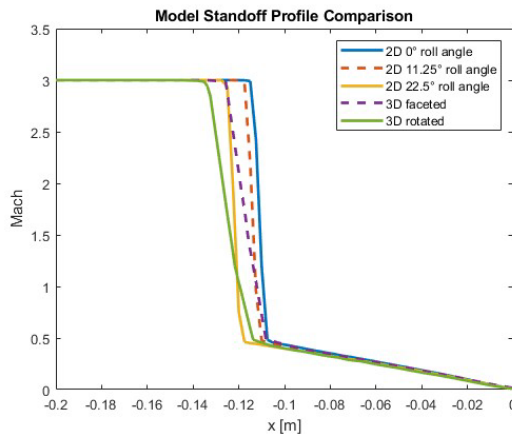b) Model Pressure profile b) Model Shield Pressure Profile

Figure 34. Model standoff profile comparison

A comparative analysis of the CFD results between the 3D faceted model and the 0° roll angle rotated model was conducted and presented in figures 35 and 36, revealing some differences in aerodynamic behavior. In figure 35, the rotated model's C_A exhibited a similar decrease rate as the faceted model, with only a 1% difference in the results. The C_N increased, and the C_m decreased as the AOA increased, with both results aligning as expected. However, at an AOA of 5°, the C_l and C_n began to show a divergence between the models result. Nevertheless, the difference in simulation results was around 5×10^{-5}, which is a negligible value that would not significantly impact the overall vehicle performance.
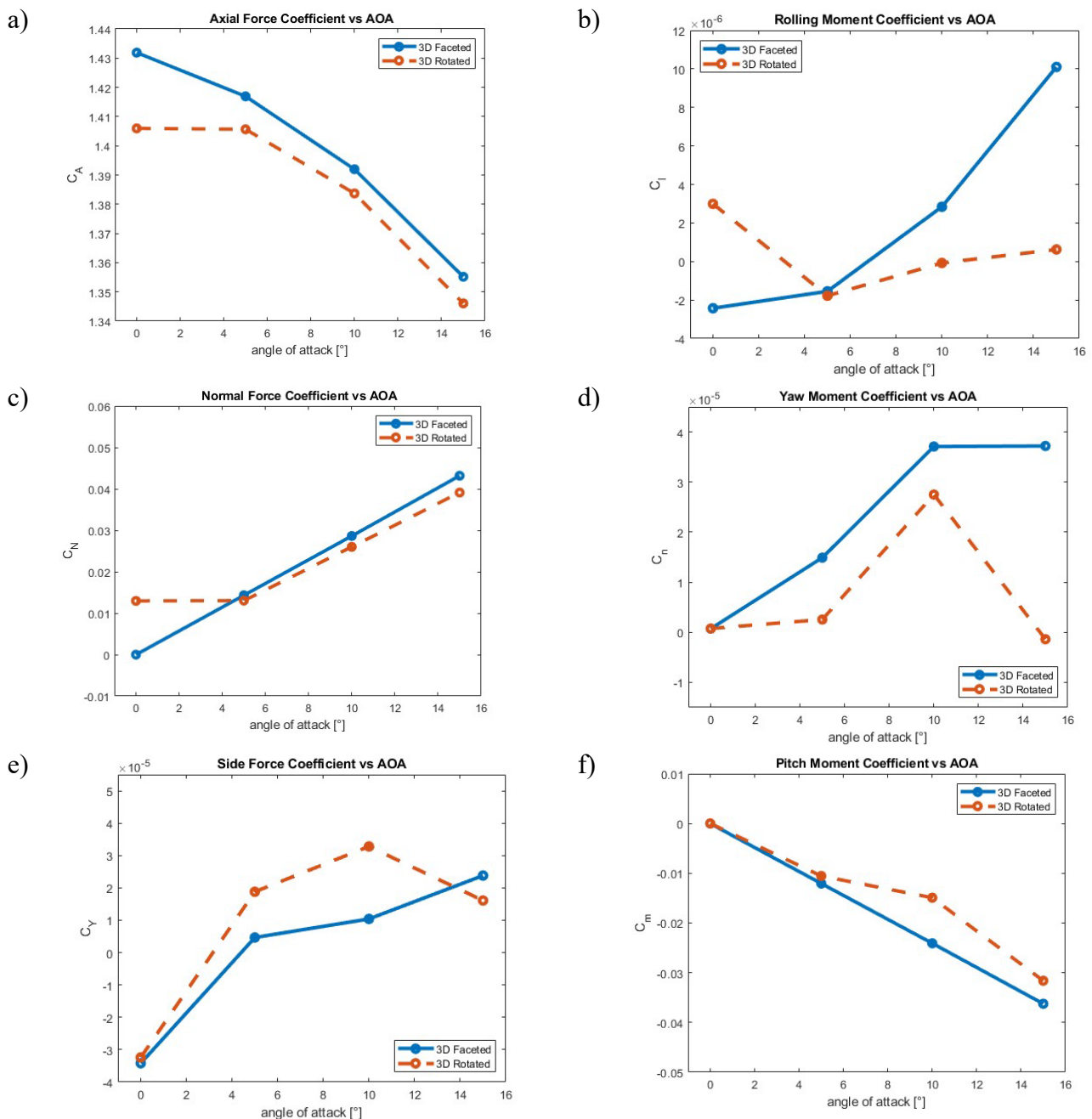

Figure 35. 3D faceted and 3D rotated model comparison

In Figure 36, the comparison of CoP coordinates revealed significant changes as the AOA increased. Although the z-direction differences were small within the range of 10^{-5}, the trend showed the CoP shifting further with the 3D faceted model. This indicates that the SR-1 model experienced more force on its forebody, even on a smaller scale, compared to the rotated model. The differences observed in the coefficients and CoP coordinates suggest variations in aerodynamic performance, but the overall impact on the vehicle's behavior appears to be relatively small.
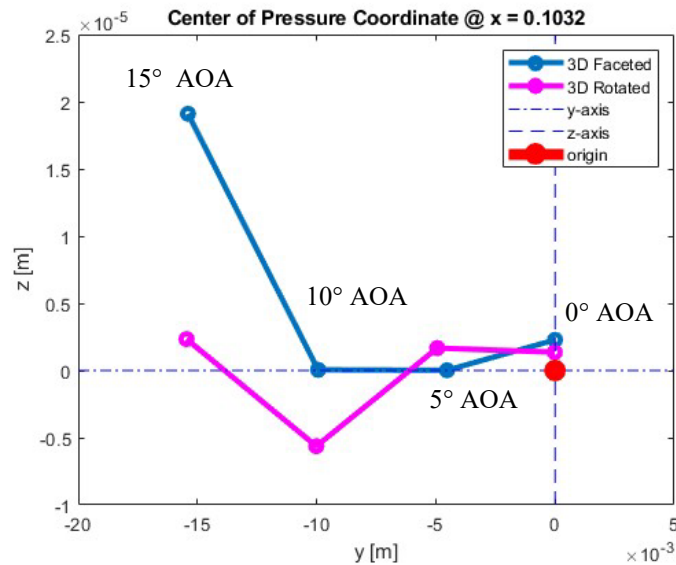

Figure 36. Faceted model vs rotate model on center of pressure location

When comparing the NASA baseline results in Table 8, the 3D faceted model overall simulation C_A result has less than a -5% difference, while C_N and C_m show differences within $\pm 7\%$ at all of the AOA. In contrast, the 3D rotated model result exhibits a consistent percentage difference compared to NASA baseline, with an approximate 3% difference. Although the 3D faceted model has a higher overall aerodynamic effect by the forebody than 3D rotated model, these force and moment would not be able to create a significant effect on the vehicle. This indicated the extended flow from forebody to aft body would be critical to estimate the aerodynamic effect on the vehicle.

Table 8. 3D model result comparison table

	NASA	3D faceted	% difference	3D rotated	% difference
0° AOA					
C_A	1.4561	1.4319	-1.6%	1.4059	-3.4%
C_N	-3.7712e-05	-1.6940e-05	-50.0%	5.0367E-05	-233.5%
C_m	7.3020e-06	-5.71e-06	-21.7%	2.8534E-05	+289.9%
10° AOA					
C_A	1.4271	1.3919	-2.4%	1.3837	-3.0%
C_N	0.0268	0.02862	+6.9%	0.0260	-2.8%
C_m	-0.0223	-0.0241	-6.6%	-0.0149	-33.6%
20° AOA					
C_A	1.3435	1.291 41	-4.9%	1.2880	-3.0%
C_N	0.0540	0.05826	+7.3%	0.0519	-2.8%
C_m	-0.0455	-0.04893	-7.0%	-0.0394	-33.6%

3.4 3D Transient Simulation Result

During the SR-1 experiment, the ADEPT SR-1 achieved its peak speed of Mach 3 at t = 250s and subsequently decelerated to Mach 0.8 within 30 seconds of flight. This rapid change in spacecraft environment necessitated a timed simulation to obtain a more accurate response of the SR-1 shield. The transient state simulation enables the model to simulate flow with time-dependent characteristics and observe the spacecraft's behavior over the given time frame. Considering the sudden change of force can create strong moments and lead to other chain reactions, the objective of this simulation is to ensure no dramatic force changes when the vehicle reaches a certain within a short time. For the simulation, a time frame of 1 second with 200 time-steps was set, and each time step underwent approximately 300 iterations to ensure reliable results. Figure 37 displays the outcome of the SR-1 front shield in a 1-second Mach 3 flow field, incorporating the previous steady-state results. Due to the limited availability of public SR-1 data, the information presented below represents an average estimated result at its peak Mach state based on figure 12.

In Figure 37, the model experienced the most force and moment spike at 0.05 seconds and tended to become stable after 0.5 seconds of the simulation. The C_A reached to 2.1 at t = 0.05s and remained at 1.52 for 0.1 second. Within this 0.2 second, the faceted model reached a higher result than SR-1 at the same position and speed, this indicated the spike of flow change could happen and able create a small pitch moment in this short period of time as shown in figure 37f. The C_n shows a negative spike at 0.05 seconds, corresponding to the axial force spike. The transient simulation result shows slightly different C_n and C_m compared to the steady result, which is expected since it falls within the range of 0° and 5° AOA. However, other CFD steady-state results match the transient simulation result, and NASA's estimated results are similar as well. The C_l and C_m values fluctuate between 3×10^{-3} and -3×10^{-3}, indicating that these two moments were not significant enough to impact the aerodynamics of the shield significantly.

Testing the SR-1 forebody revealed that the aerodynamic performance of the front shield alone cannot generate enough side force or moment to induce vehicle auto rotation. In the meantime, there are no extreme force changes when the vehicle first contacts the flow within a short time which means the unpredict roll rate increase is unlikely caused by a sudden change in force. However, the uncertainty of the aft body flow generated by the octagon-shaped edge will be critical for the overall aerodynamics of the vehicle, and it is recommended to include a simulation that encompasses the complete aft body flow.
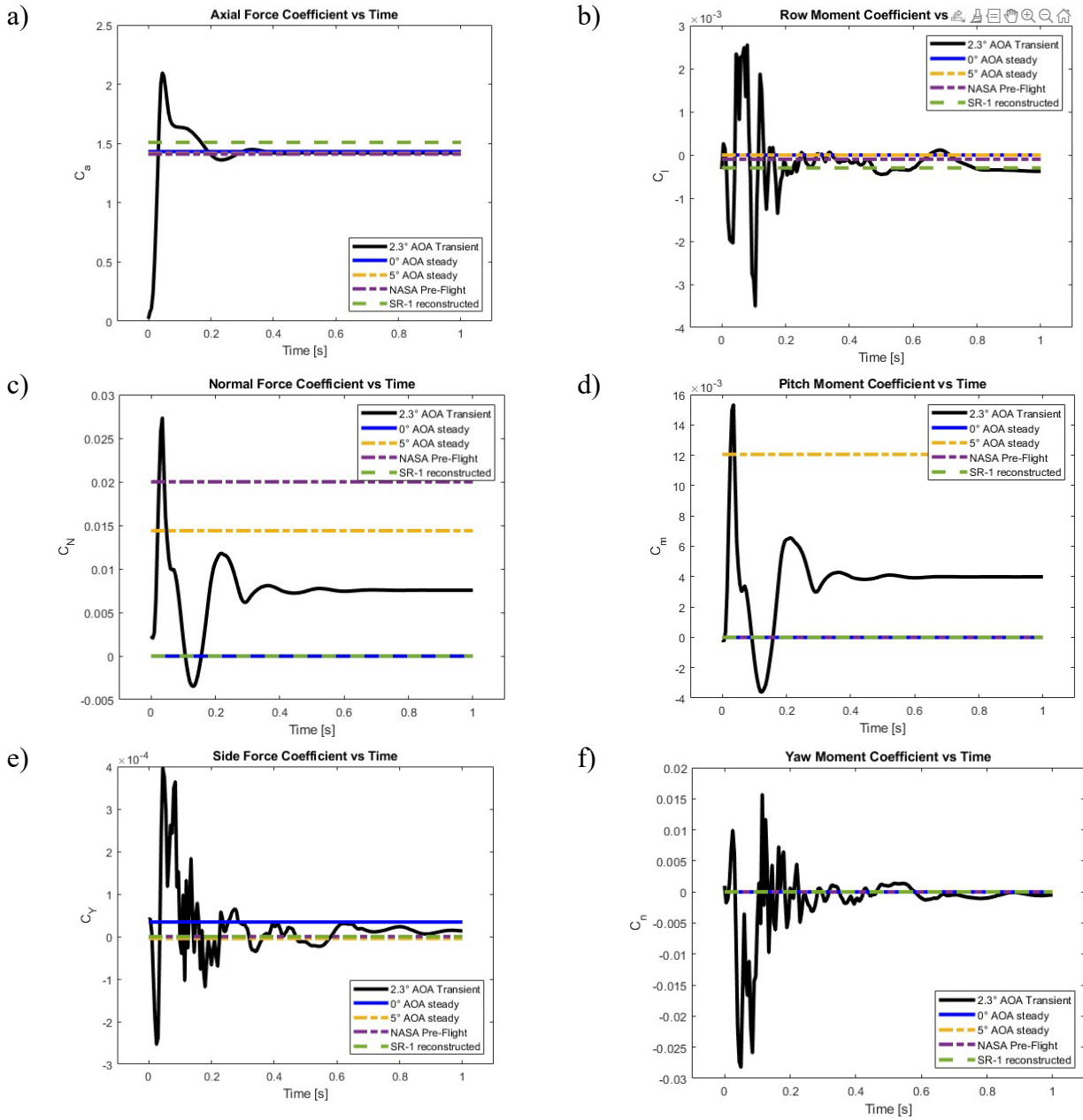
a) **Axial Force Coefficient vs Time**

b) **Row Moment Coefficient vs**

c) **Normal Force Coefficient vs Time**

d) **Pitch Moment Coefficient vs Time**

e) **Side Force Coefficient vs Time**

f) **Yaw Moment Coefficient vs Time**

Figure 37. 3D faceted model transient simulation result

3.5 Aft body Transition Test Result

Given the absence of significant results from the forebody of the SR-1 shield, it is possible that the aft body aerodynamics is a more critical factor contributing to the unexpected increase in roll rate during the SR-1. Further analysis of flow transition between the forebody and aft body may provide more insight into the effects of the forebody geometry on the aft body aerodynamics.

3.5.1 0° AOA result

All the test results from the previous simulations were revisited to investigate the flow conditions at the outlet of the forebody model which would be in the inlet conditions for an aft body analysis. For the 2D results, the data ranged from the nose of the shield at x = 0.12m and y = 0 m, along the surface of the forebody, to the end of the flow field and a similar set of data from a position 0.01m further aft, as illustrated in Figure 38. In the case of the 3D results, the data spanned from one side to the other of the flow field, excluding the model surface data. The data range was also situated at x = 0.12m and 0.13m, as depicted in Figure 39.
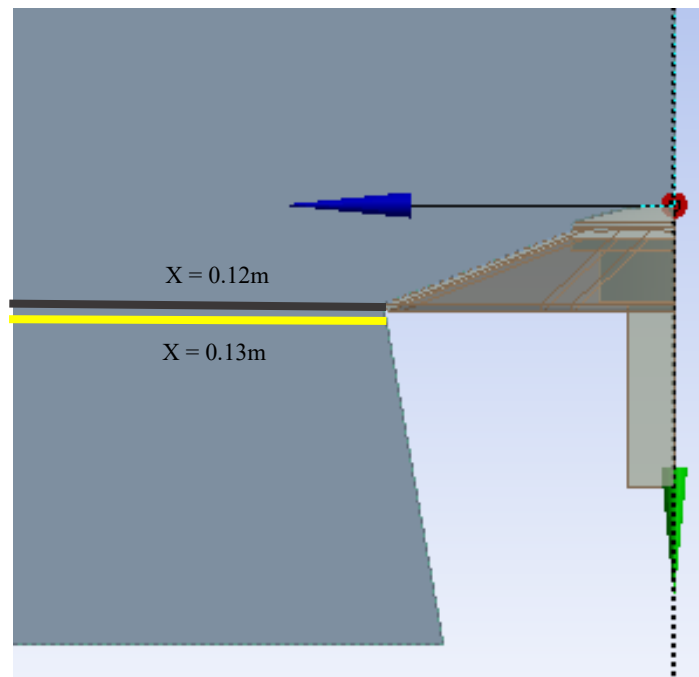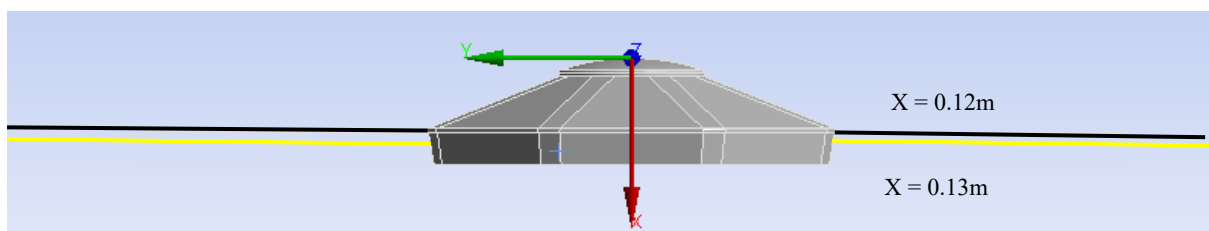

Figure 38. 2D model data collection range

Figure 39. 3D model data collection range side view

Figures 40 and 41 depict a comparison of static pressure contours between the two models at positions x = 0.12m and x = 0.13m. The flow distribution around the model, as anticipated, appears uniform, devoid of any pressure spike areas for both models and locations. Notably, an encompassing low-pressure zone, resembling a ring, becomes apparent around the model. This phenomenon suggests the potential onset of separation, progressively intensifying until it converges with the end of the shock wave. This observation raises the possibility that the aft body will be influenced by distinct forces arising from the turbulent and uncertain flow, particularly within the vehicle's aft body region.
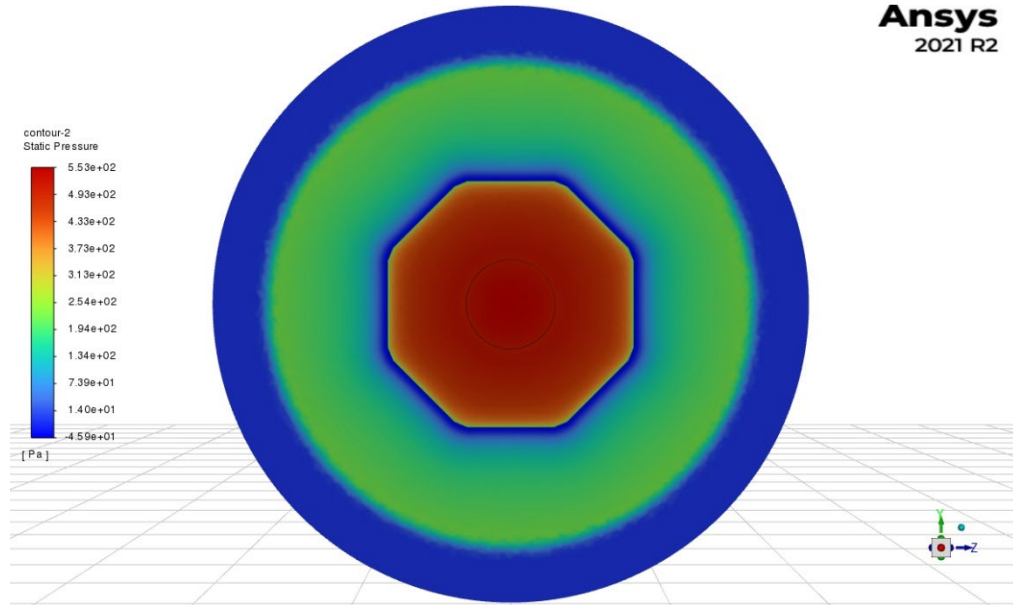
a)

b)
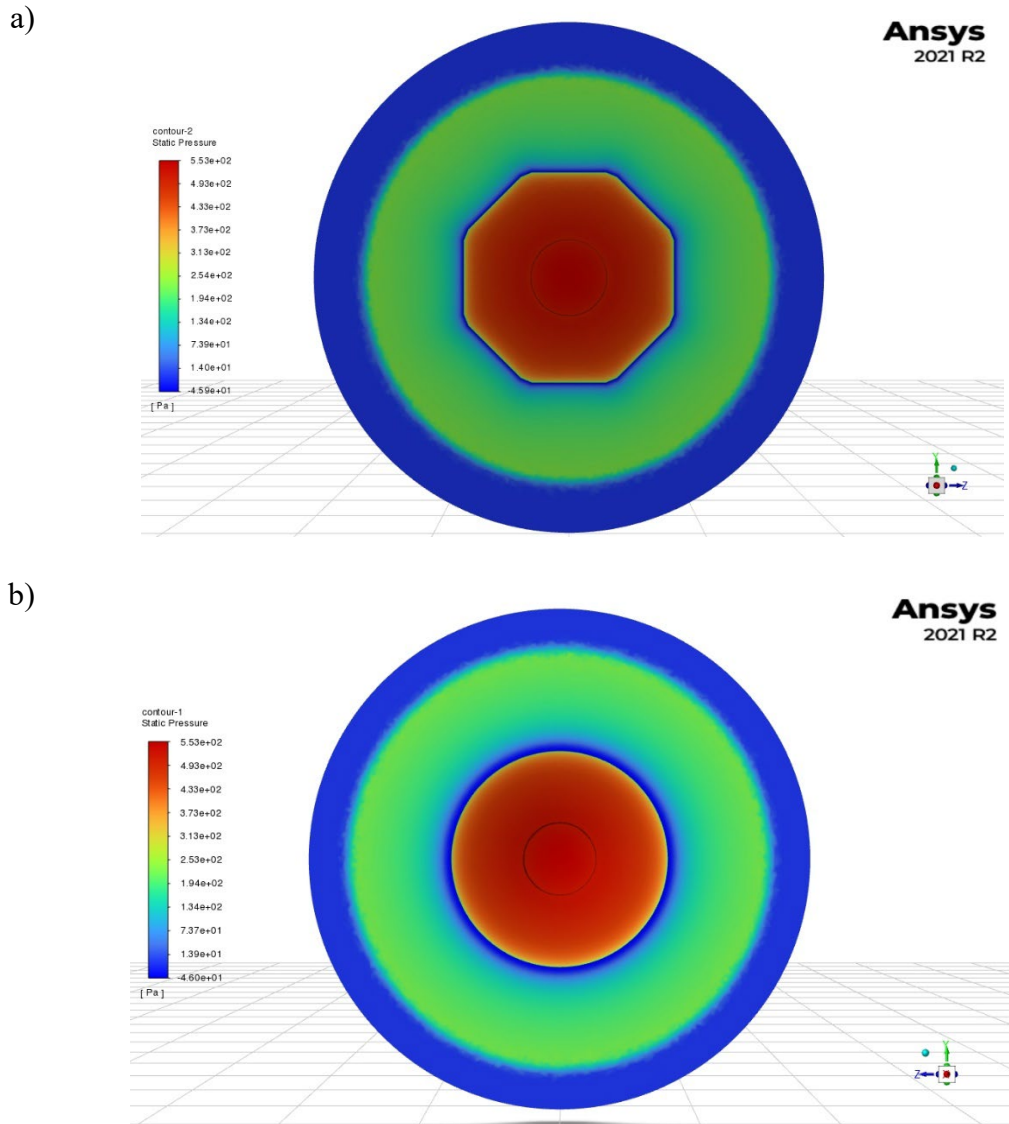
Figure 40. Model 0° AOA static pressure profile top-view at x =0.12m
a) 3D Faceted Model   b) 3D rotated model

a)

b)

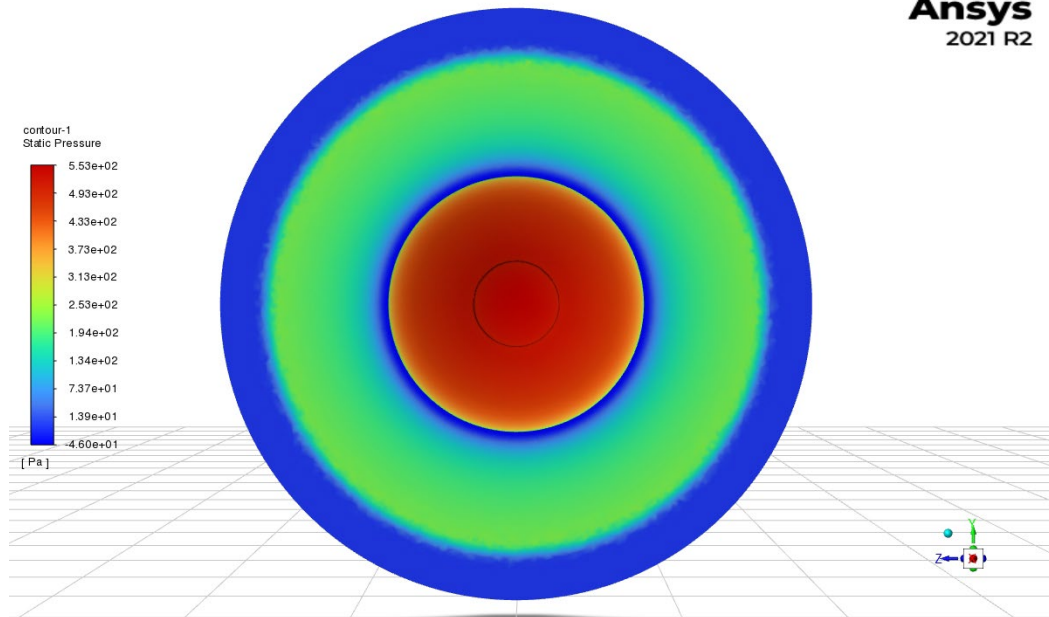

Figure 41. Model 0° AOA static pressure profile top-view at x =0.13m
a) 3D Faceted Model b) 3D rotated model

The following figures 42 to 44 describe the flow conditions for both x = 0.12m and 0.13m at 0° AOA. Considering this result at 0° AOA, force in 3D model would be symmetrical between positive and negative region of the model in figure 18, and the coordinate changes according to its radius. The static pressure data shows a stable and converged trend before R/R_b of 1.8 within the shock wave for x = 0.12m, and rapid decrease with a constant rate after R/R_b of 1.8 when it reaches the shock in figure 42a. Small differences between models can be seen in between R/R_b of 1.8 and 2 with the 22.5° roll angle (RA) 3D faceted model begin diverging first. Similar data between models shows in Mach, and temperature data, and this indirectly shows a similarity within shock between RA at x = 0.12m.

Upon reaching x = 0.13m, the 11.25° RA 3D faceted model displays notable differences compared to other models within the shock region between R/R_b 1 and 1.5. The difference in envelope shock distance between different models becomes evident between R/R_b of 1.8 and 2.1, as shown in Figure 42b. This difference in y direction shock distance is more pronounced in the Mach distribution with the change estimated around 0.02m depicted in Figure 43b, where varying roll angles lead to distinct shock distance in the transition flow. In the meantime, the static pressure and Mach result shows a similarity between models and roll angles. Considering the influence of different radii for roll angles, it is plausible that specific sections of the shield may generate a wider shock envelope, introducing more flow perturbation in the aft flow.
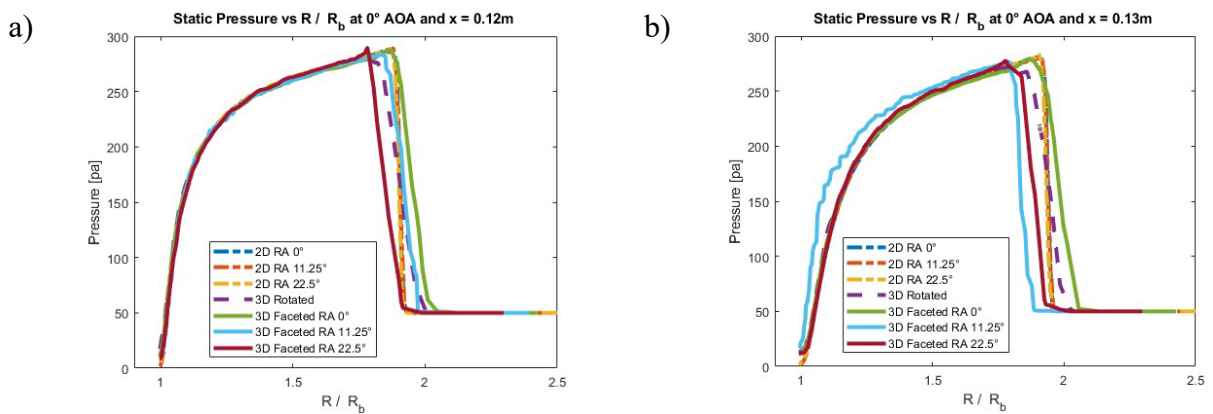
a)
b)

Figure 42. 2D and 3D models static pressure profile at 0° AOA
a) X = 0.12m b) X = 0.13m

a)
b)
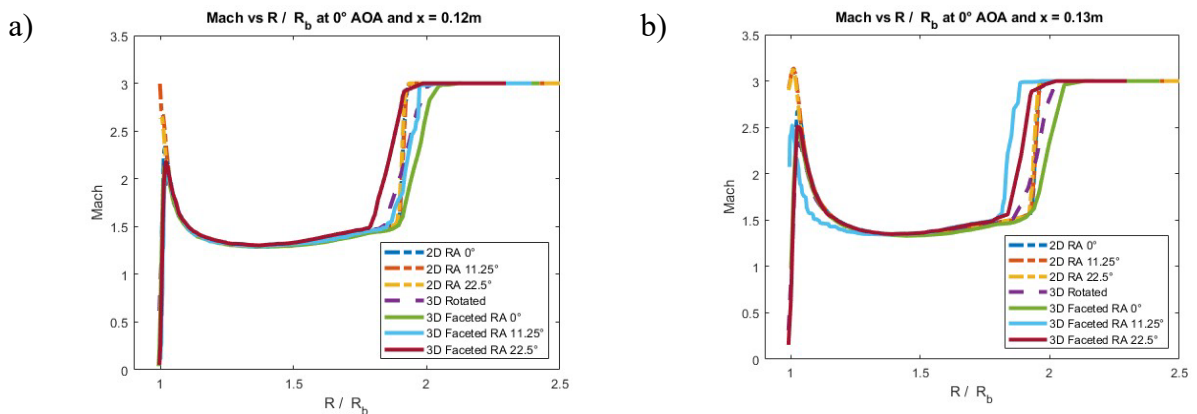

Figure 43. 2D and 3D model Mach profile at 0° AOA
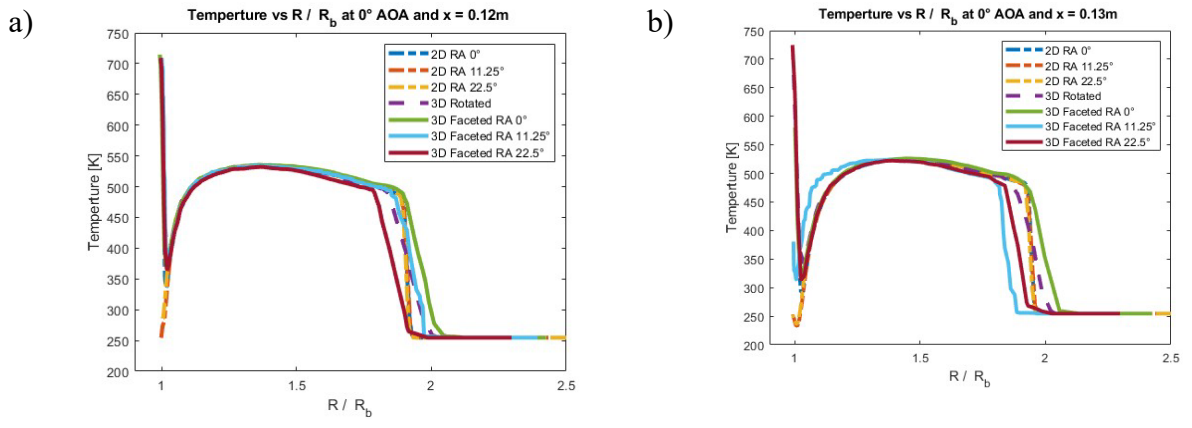a) X = 0.12m b) X = 0.13m

Figure 44. 2D and 3D model temperature profile at 0° AOA
a) X = 0.12m b) X = 0.13m

3.5.2 Test Result at 5° AOA

In the subsequent section, the collected results pertain to a 5° angle of attack (AOA) derived from the preceding simulation. The recreation of an AOA flow necessitates the assessment of axial and normal forces. The dataset encompasses a range from -y to +y (illustrated by the black line), where the normal force flow traverses from the negative y region to the positive y direction, as visualized in Figure 45b below. At the same time, the outcomes along the z-axis (illustrated by the blue line) are also taken into account to demonstrated possible aerodynamic effect with AOA flow.

a)

b)

Free stream

X = 0.12m

X = 0.13m

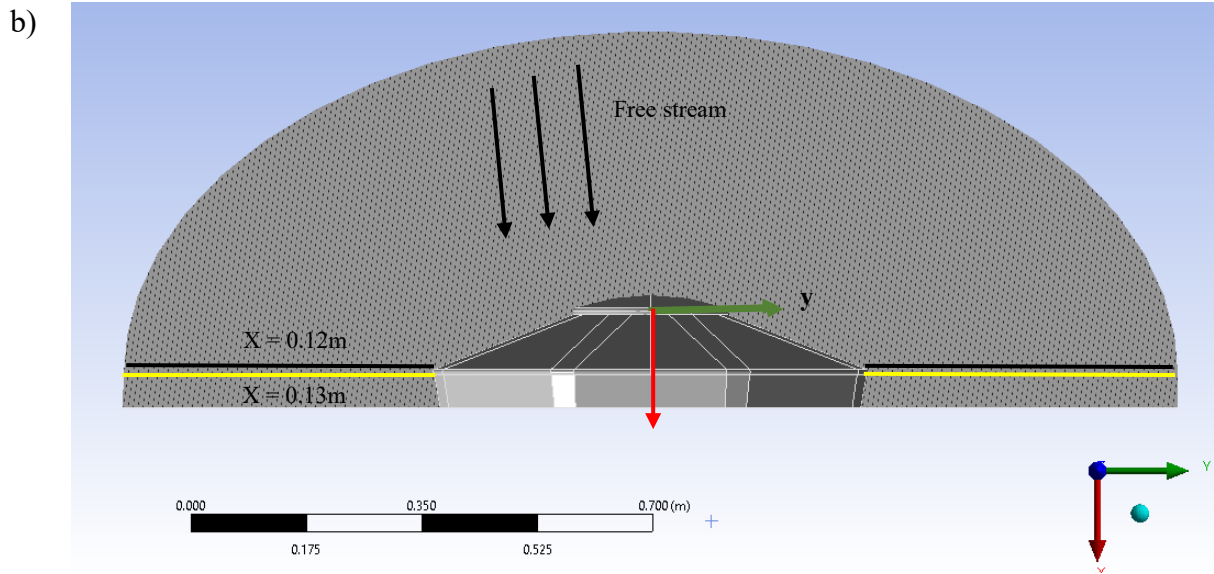| 0.000 | | 0.350 | | 0.700 (m) |

0.175   0.525
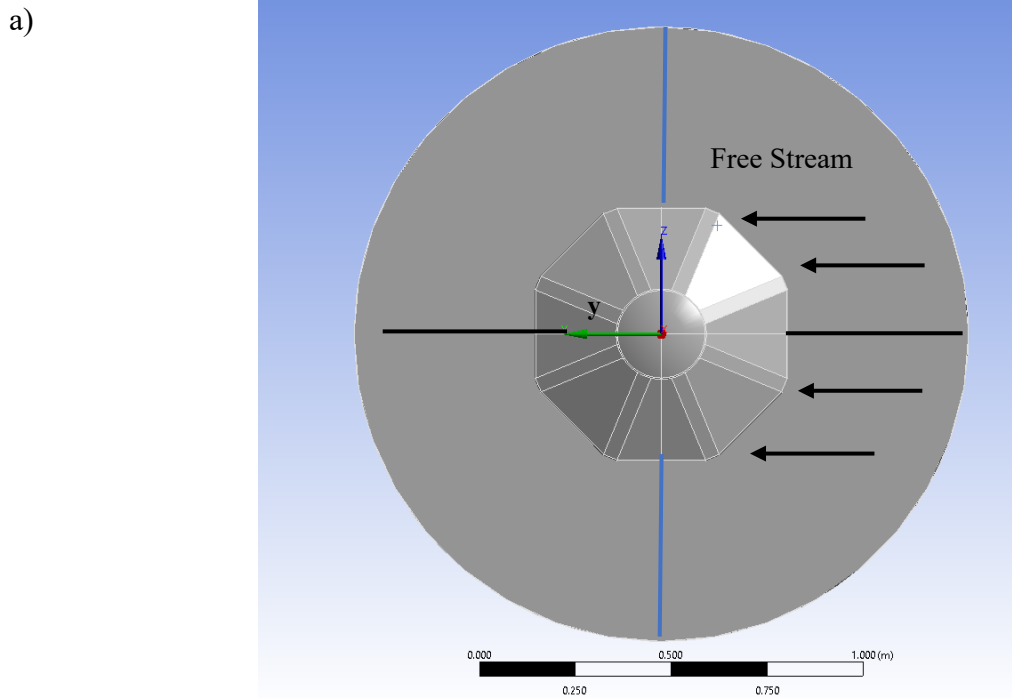
Figure 45. Model data collection location with flow direction
a)   Upper view b) side view

The subsequent figures present a juxtaposition of static pressure contours between the 3D faceted and rotated models at positions x = 0.12m and x = 0.13m at a higher angle of attack. With flow entering from the negative y-direction, discernible pressure disparities become apparent on the lower and upper sections of the shield, reflected by differing shock distances. This contrast is visually depicted in figures 46 and 47. Notably, the low-pressure region, akin to a blue ring encompassing the model, exhibits an augmented thickness as x increases or extends rearward. Both sets of pressure contours notably adhere to anticipated flow patterns and shock wave dynamics within the context of AOA-induced flows.
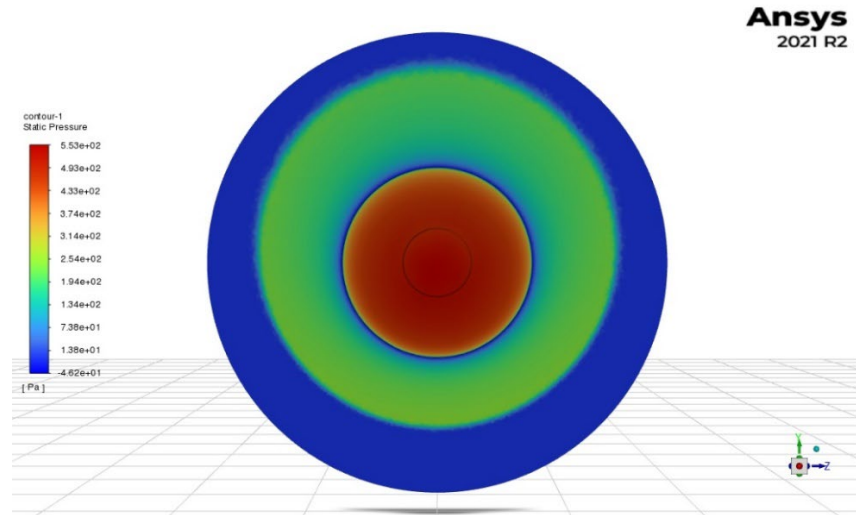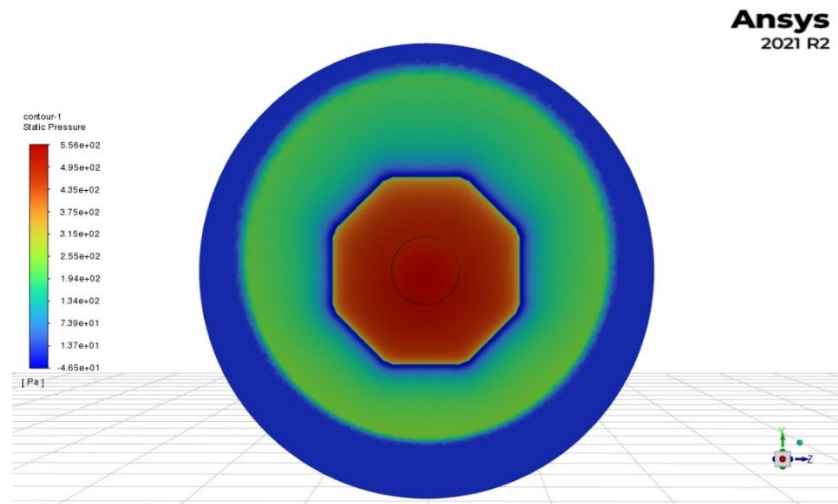
a)
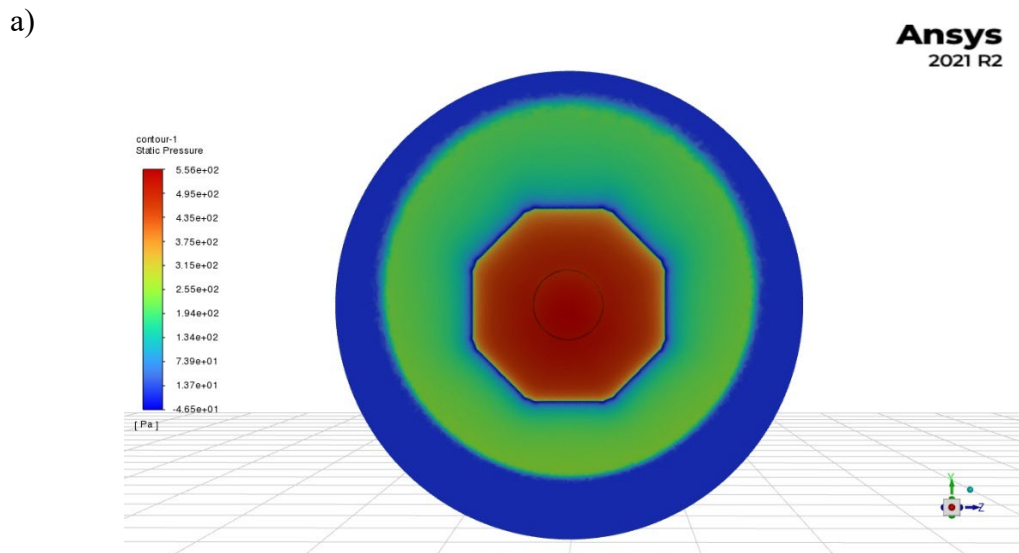
b)

Figure 46. Model 5° AOA static pressure profile top-view at x =0.12m
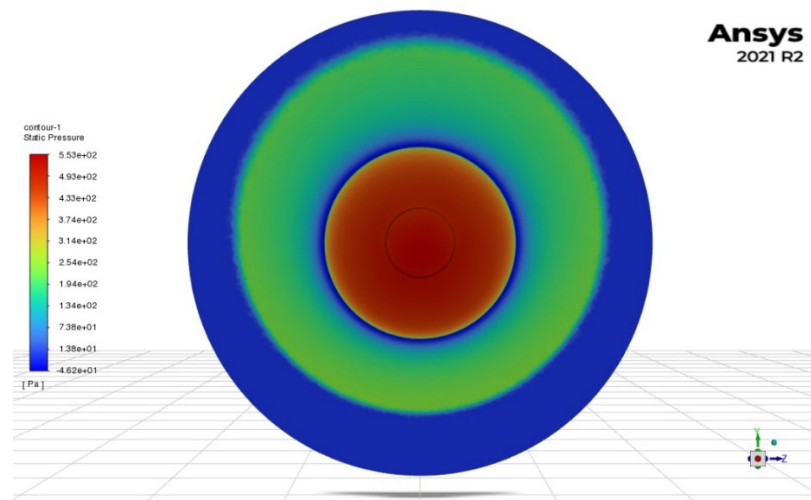a)   3D Faceted Model   b) 3D rotated model

a)

b)

Figure 47. Model 5° AOA static pressure profile top-view at x =0.13m
a)   3D Faceted Model   b) 3D rotated model

The positive or negative R/R$_b$ region indicated the positive or negative region for either y or z axis served as coordinate of the shield. Figure 48 underscores this notion, wherein the model's static pressure exhibits elevated values within a narrower R/R$_b$ range in the negative R/R$_b$ region, in perfect alignment with expectations. This phenomenon directly arises due to the anticipated entry of normal force flow from the negative direction into the flow field. Conversely, on the opposing side of the shield, the encounter with the shockwave prompts the shield to experience reduced force exertion over an extended R/R$_b$ range, in contrast to the negative region Mach and temperature result in figure 49 and 50 on y axis shows a similar pattern with smaller "bucket" in the negative region than position region.

In regard to the z-direction results, both the negative and positive regions manifest symmetrical outcomes for pressure, temperature, and Mach, aligning with expectations due to the absence of lateral forces in this simulation. All models consistently exhibit similar outcomes along either the y or z direction, regardless of changes in roll angle or the implementation of a rotated model. This observation underscores that alterations in the shield's roll angle do not induce significant changes in the aerodynamic impact on the front shield alone.

However, discernible variations in shock distances across different roll angles within the z and y axes are evident in the findings presented in Section 3.5. These disparities manifest within the R/Rb ratio range of 2 to 2.2, signifying that some flow emanating from specific edges extends farther outward than others. This divergence in flow paths could potentially lead to unexpected merging, with the marginal 0.2 ratio variance corresponding to a mere 0.07m discrepancy. Given the elongated aft body, the implications of flow merging within this region remain uncertain, particularly under the influence of AOA-induced flows. Further investigation into the behavior of the SR-1 vehicle is necessary to comprehend potential additional pressure effects along the cargo's sides. Consequently, investigation of the aft body flow is merited.
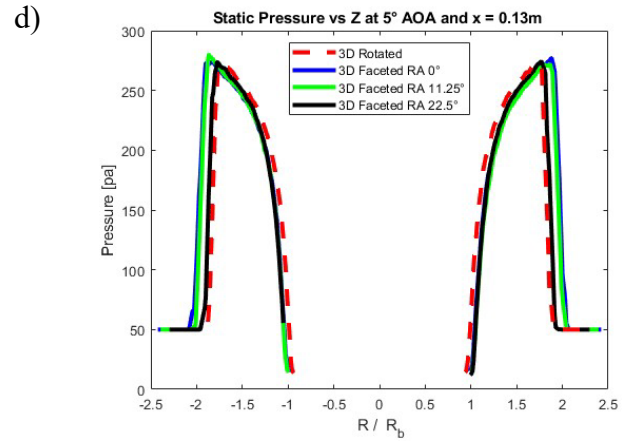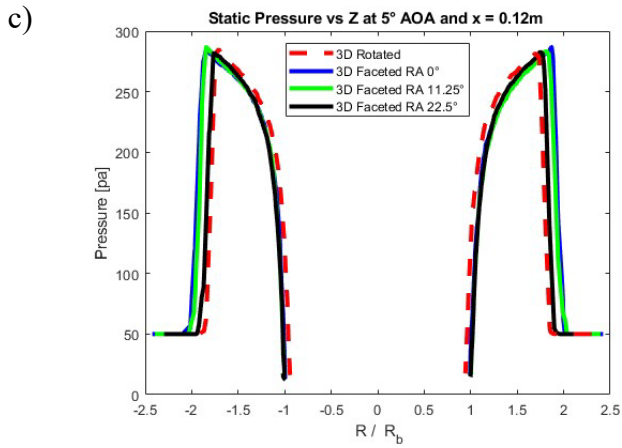
a)

b)
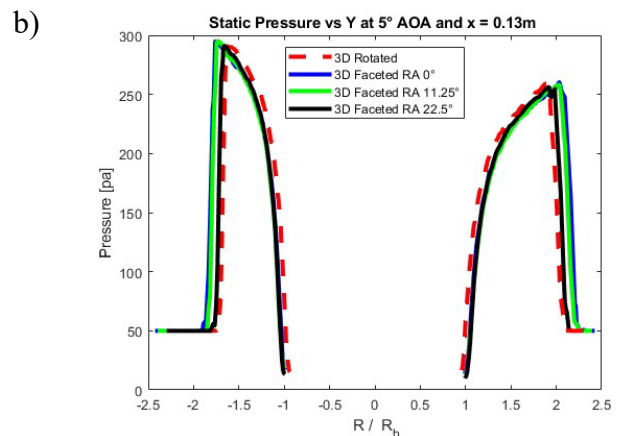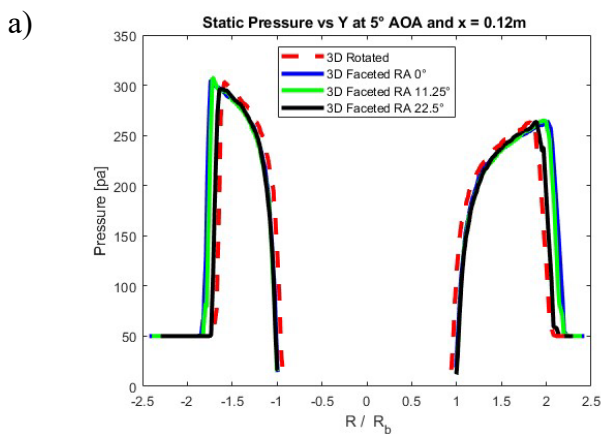
Figure 48. 3D model static pressure profile at 5° AOA
a) Y at x = -0.12m b) Y at x = -0.13m c) Z at x = -0.12m d) Z at x = -0.13m
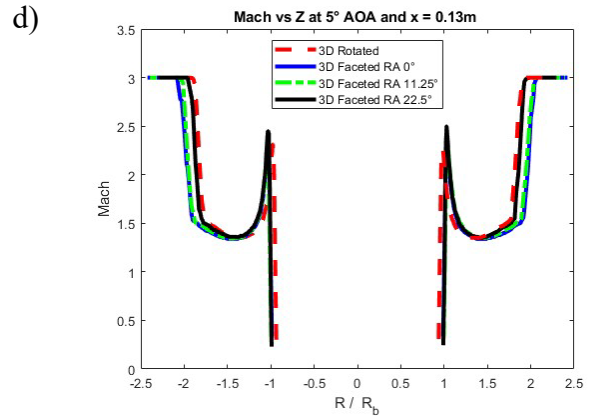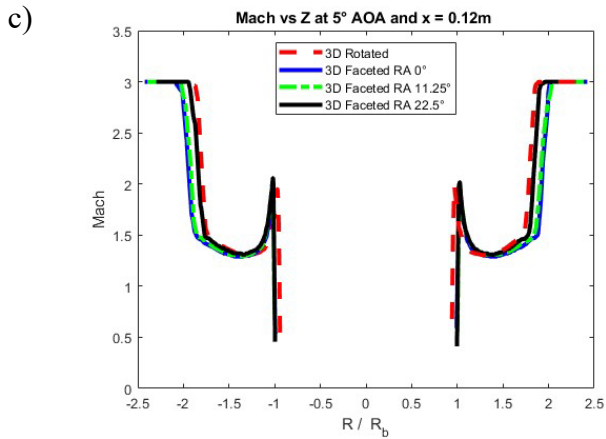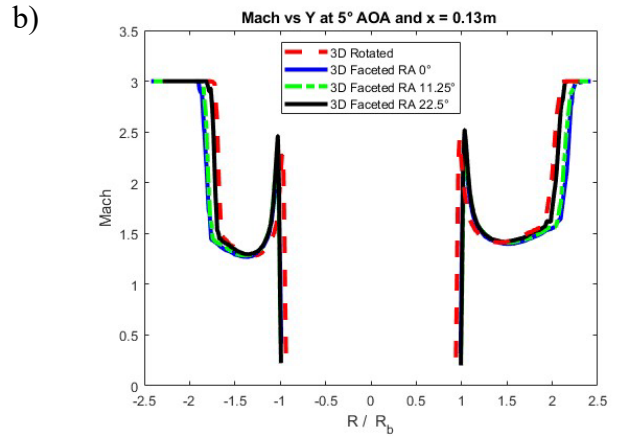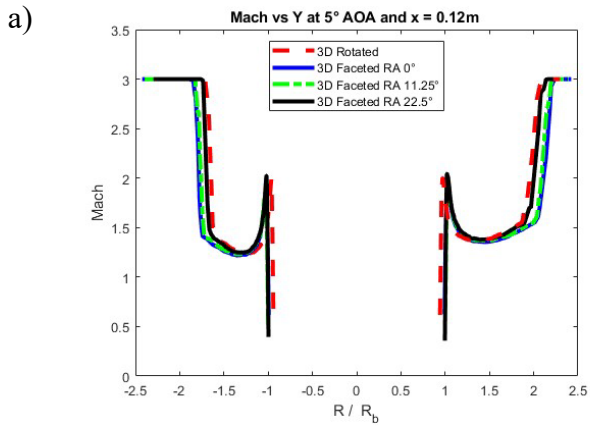

Figure 49. 3D model Mach profile at 5° AOA
a) Y at x = -0.12m b) Y at x = -0.13m c) Z at x = -0.12m d) Z at x = -0.13m
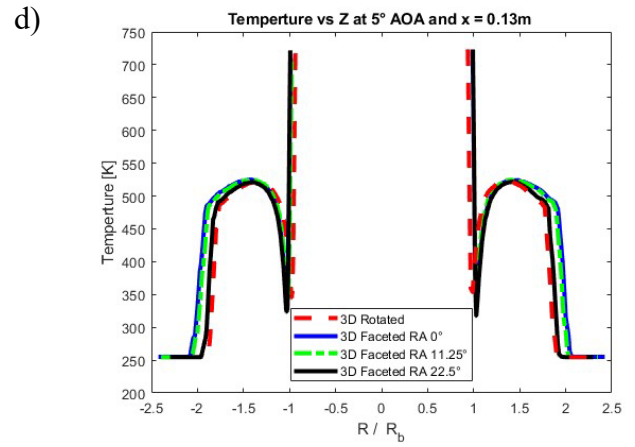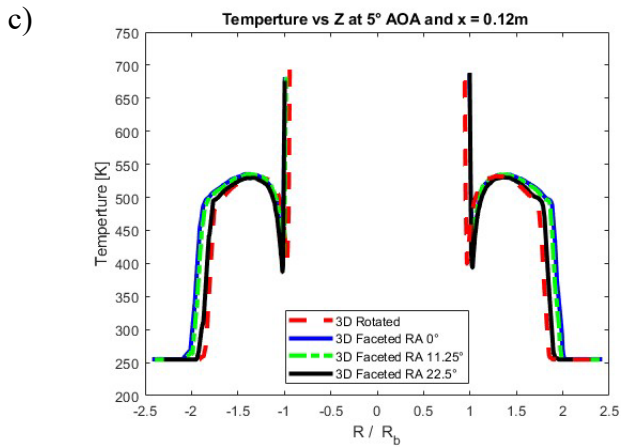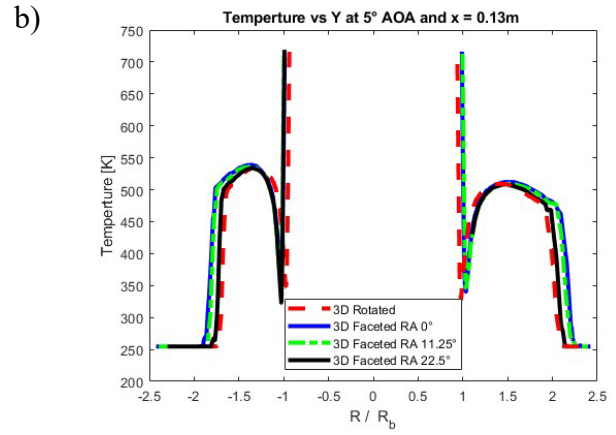
Figure 50. 3D model temperature profile at 5° AOA
a) Y at x = -0.12m b) Y at x = -0.13m c) Z at x = -0.12m d) Z at x = -0.13m
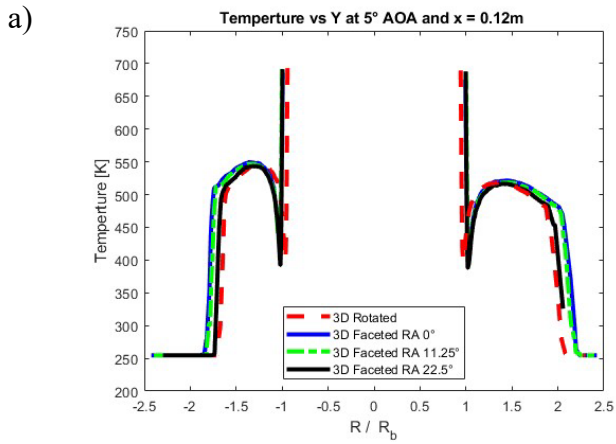
4 Conclusion and Future Work

This simulation was conducted to explore the potential existence of additional forces acting on the ADEPT SR-1 front shield which were not accounted for in NASA's pre-flight CFD analysis. Utilizing 2D axisymmetric and 3D model simulations, the aerodynamic investigation demonstrated that no significant unexpected forces or moments were generated by the forebody of the SR-1 shield in supersonic conditions due to NASA's use of axisymmetric assumptions. Moreover, comparisons between steady and transient simulations revealed that the rib structure of the shield had minimal influence on generating additional side forces, and variations in the roll angle had negligible effects on overall aerodynamic characteristics.

Upon scrutinizing the transition flow of both models, a marginal variation in shock distances emerges within their respective results. This hints at the possibility that the aft body's aerodynamics has a more pivotal influence on the spacecraft's stability and trajectory estimation than its front shield. Subsequent endeavors in CFD analysis should be directed towards comprehending the intricacies of the aft body, encompassing diverse velocities and environmental conditions contingent on flows around differing radii edges. The suspicion lingers that the peculiar spin rate encountered in the SR-1 flight experiment may find its origins in the aerodynamic effects experienced by the aft body. The complexities introduced by the octagon-shaped edge accentuate the need for an extensive-scale CFD exploration of the SR-1's aft region. It is advised to enhance geometric precision and meticulously tailor the computational grid to emphasize the aft body's adjacent flow area in the CFD model. Addressing these aspects can lead to a more precise representation of the SR-1 shield's behavior during reentry, ensuring reliable results for future missions and spacecraft designs.

Reference

[1]   Smith, B. P., Cassell, A. M., Kruger, C. E., Venkatapathy, E., Kazemba, C. D., and Simonis, K. R., "Nano-ADEPT: An Entry System for Secondary Payloads," *IEEEAC* Paper 7119095, March 2015.

[2]   Wercinski, P. F., "ADEPT Sounding Rocket One (SR-1) Flight Experiment Overview," *IEEEAC* Paper 7943889, March 2017.

[3]   Venkatapathy, E., Hamm, K., and Fernandez, I., "Adaptive Deployable Entry and Placement Technology (ADEPT): A Feasibility Study for Human Missions to Mars", Published Online:5 Nov 2012, https://doi.org/10.2514/6.2011-2608

[4]   Dutta, S., and Green, J. S., "Flight Mechanics Modeling and Post Flight Analysis of ADEPT SR-1," AIAA Paper 2019–XXXX, January 2019.

[5]   Ernst-Heinrich Hirschel, Claus Weiland, Aerothermodynamic Design Problems of Hypersonic Flight Vehicles, Springer, 2008.

[6]   Prabhu, D., and Saunders, D.A., "On heatshield shape for Mars Entry Capsules", AIAA paper, January 2021, DOI:10.2514/6.2012-399

[7]   Marla, A., and Carol, D., "Planetart Mission Entry Vehicles Quick Reference Guide. Version 3.0", NASA , SP-2006-3401, January 2006

[8]   Kirk, D. B., Intrieri, P. F., and Seiff, A., "Aerodynamic Behavior of the Viking Entry Vehicle: Ground Test and Flight Results," *Journal of Spacecraft and Rockets*, Vol. 15, No. 4, 1978, pp. 208-212.

[9]   Mitcheltree, R. A. , Wilmoth, R. G., Braucjmann, J. G., Greene, F. A.,"Aerodyanmic of Stardust Sample Return Cpasule", NASA Lanely Research Center, Hampton, Virginia

[10]   Olds, A. D., Beck, R. E., Bose, D. M., White, J. P., Edquist, K. T., Hollis, B. R., Lindell, M. C., Cheatwood, F. M., Gsell, V. T., and Bowden, E. L., "IRVE-3 Post-Flight Reconstruction," *AIAA* Paper 2013–1390, March 2013

[11]   White, B., Tegnerud, E., Morgan, H., Benton, J., Murbach, M., Cropper, M., DeLeon, P., Lane, R., William, M., "The SOAREX-VI Re-entry Flight Test Experiment", International Planetary Probe Workshop Conference Proceedings, June 27,2008

[12]   Cassell, A. M., Smith, B. P., Wercinski, P.F.,Ghassemieh,S.M., "ADEPT, A Mechanically Deployable Re-Entry Vehicle System, Enabiling Interplanetary CubeSat and Small Satellite Missions", AIAA Paper SSC18-XII-08, August 2018

[13]   Arnold, J.; Laub, B.; Chen, Y.-K.; Prabhu, D.; Bittner, M.; Venkatapathy, E., "Arcjet Testing of Woven Carbon Cloth for Use on Adaptive Deployable Entry Placement Technology" IEEE Aerospace Conference 2013

[14]   Dutta, S., Karlgaard, C. D., Korzun, A.M., Green, J.S., Tynis, J.A., Williams, J.D., Yount, B., Cassell, A.M., and Wercinski, P.F., " Adaptable Deployable Entry and Placement Technology Sounding Rocket One Modeling and Reconstruction", *Journal of Spacecraft and Rocket, Vol.59* No.1, January 2022

[15]   Korzun, A., McDaniel, R., Karlgaard, C., and Tynis, J., "Aerodynamics for the ADEPT SR-1 Flight Experiment," *AIAA SciTech 2019, AIAA Atmospheric Flight Mechanics Conference,* San Diego, CA, 2019.

[16]   Venkatapathy, E., Hamm, K., and Fernandez, I., "Adaptive Deployable Entry and Placement Technology (ADEPT): A Feasibility Study for Human Missions to Mars", Published Online:5 Nov 2012, https://doi.org/10.2514/6.2011-2608

[17]   Dec, J.A. "Three dimensional finite elements ablative thermal reposonse analysis applied to heat shiled penetration design", May 2010

[18]   Smith, B. P., Yount, B., Kruger, C., Brivkalns, C., Makino, A., Cassell, A., Zarchi, K., McDaniel, R., Ross, J., Wercinski, P.,Venkatapathy, E., Swanson, G., and Gold, N., "Nano-ADEPT Aeroloads Wind Tunnel Test," IEEEAC Paper 7500719, March2016.

[19]   Tynis, J. A., and Karlgaard, C. D., "Reconstruction of the Adaptable Deployable Entry and Placement Technology Sounding Rocket One Flight Test," AIAA Paper 2019–XXXX, January 2019.

[20]   Sébastien Deck, Philippe Duveau, Paulo d'Espiney, Philippe Guillen, "Development and application of Spalart–Allmaras one equation turbulence model to three-dimensional supersonic complex configurations", *Aerospace Science and Technology, Volume 6*, Issue 3, 2002, Pages 171-183, ISSN 1270-9638, https://doi.org/10.1016/S1270-9638(02)01148-3.

[21]   Hills, P. J., and Korzun, M. A., personal communication, October 2023.

[22]   "ADEPT's Spiderweave Material Tested at Arc Jet Facilities", NASA , August 13, 2021, https://www.nasa.gov/image-feature/ames/spiderweave-testing

Appendix A. 3D Steady Simulation Data

["AOA" " Axial Force" " Axial Force Coef " " Normal Force Coef" "Side Force Coef" "Pitch Moment Coef" "Yaw Moment Coef" "Roll Moment Coef" "Normal Force" "Side Force" "x-axis moment" "y-axis moment" "z-axis moment"]

```
0      167.70746    1.4318848    -1.69E-05     3.42E-05      7.15E-07      -5.71E-06
       -2.43E-06    -0.001984166 0.00399985    -2.43E-06     7.14E-07      -
0.000459673
5      165.7128     1.4169259    0.014318768   -4.66E-06     1.49E-05
       0.012055846  -1.55E-06    1.6746134     -0.000544732 -0.000124555
       0.001198904  0.96976998
5      165.71084    1.4148377    0.014296065   -1.43E-06     1.40E-06
       0.012031663  8.22E-07     1.6744061     -0.000167539 6.62E-05
       0.000112647  0.96924179
5      165.74218    1.4151053    0.014343572   8.22E-06      -9.50E-07
       0.012060354  -1.60E-06    1.6799704     0.000962633   -0.000128886 -7.66E-05
       0.012060354
5      165.02307    1.4148614    0.014289359   2.30E-05      -1.06E-05
       0.012035514  -1.05E-06    1.484898      0.005236126   -8.48E-05     -
0.002464554  0.96955202
5      165.70692    1.4148042    0.014279515   1.41E-05      7.31E-07
       0.012040948  -5.15E-06    1.6724677     0.001651842   -0.000414841 2.85E-06
       0.00989217
10     162.3626     1.3919678    0.02862       -1.04E-05     3.71E-05
       0.024082949  2.84E-06     3.3530796     -0.001223248 0.00022913
       0.002988355  1.9400644
10     163.0415     1.3920473    0.028671733   -2.34E-05     5.65E-05
       0.024202408  2.01E-06     3.3581357     -0.002736694 0.000161156
       0.004534778  1.9411838
10     163.04071    1.3920402    0.028615339   -8.51E-06     2.06E-05
       0.024074644  4.25E-06     3.3515306     -0.000996149 0.000342552
       0.001659453  1.9393953
10     162.36015    1.39198      0.028657063   1.69E-05      1.24E-05      0.02411
       7.55E-06     3.3564175    0.001984227   0.000600648   0.000995552  1.9427037
10     163.03223    1.3920023    0.028624896   2.17E-05      -4.52E-06
       0.016559634  8.92E-06     3.35265       0.002539738   0.001044194  -
0.000529727  1.9395234
15     158.4526     1.355176     0.043172003   -2.38 E-05    3.72E-05
       0.036240658  1.01E-05     5.0512672     -0.002784824 0.000817444
       0.002994493  2.9194601
15     157.74526    1.3523935    0.04313363    -2.31E-05     3.13E-05
       0.036238337  6.64E-06     5.0519647     -0.002709985 0.00052121
       0.002549233  2.9200776
15     158.39832    1.3524035    0.043098021   -1.30E-05     2.22E-05
       0.036196103  3.15E-06     5.0477941     -0.001517537 0.000253733
       0.001786844  2.9158708
15     158.39661    1.3523889    0.043158865   1.55E-05      5.12E-06      0.036256
       4.97E-06     5.0549202    0.001813727   0.000400371   0.000412797  2.9191386
15     157.74456    1.3524136    0.043127675   -2.38E-05     3.72E-05
       0.036240658  1.01E-05     5.0492984     0.001601827   0.001601827
       0.001746835  2.918787
20     151.48879    1.29341      0.058260379   3.33E-06      2.56E-05
       0.048879558  7.68E-06     6.8236635     0.000390105   7.68E-06      2.56E-05
       3.9376194
```